

ON THE OSCILLATIONS OF JUPITER
AS OBSERVED BY VOYAGER 2

by

WESLEY BURR

A thesis submitted to the
Dept. of Mathematics and Statistics
in conformity with the requirements for
the degree of Master of Science

Queen's University
Kingston, Ontario, Canada
December 2007

Copyright © Wesley Burr, 2007

Abstract

Data recorded from Voyager 2 in 1979 during closest approach to Jupiter is prepared and analyzed for evidence of Jovian modal forcing. Comparisons are drawn between the data set in question and previously performed analysis by Mosser *et al.* [27], [29], [6] and also to the models presented by Gudkova and Zharkov in [19].

The theory of stationary processes and multitaper spectrum estimation are employed extensively in the analysis, along with intensive use of the harmonic frequency variance test as a tool for separating signal from noise.

The splitting of low-order p-modes is briefly examined and found to be in-line with that discovered earlier by Mosser *et al.*.

Acknowledgments

I must acknowledge my family, who have patiently put up with my procrastination, general ill-nature, and random babbling about Jupiter for the last year. I especially thank my wife, Belinda, without whom this thesis would not have been completed. Her support has made all the difference.

I also must acknowledge the care and support that Dr. David Thomson and his wife, Maja-Lisa, have given to me over the last three years. Their support helped me get through the program, and arrive at a point where completing this thesis became a real possibility.

Contents

Abstract	i
Acknowledgments	ii
Contents	iii
List of Tables	vi
List of Figures	vii
1 Introduction	1
2 Background on Jupiter Research	3
2.1 Early Work	3
2.2 Asymptotic Approximations	4
2.3 An Additional Model	4
2.4 The First Proposal	5
2.5 Tentative First Observation	5
2.6 Theory Catches Up with Observation	6
2.7 Further Attempts	7
2.8 Radio Period Fixed	8
2.9 Results since 1999	8
2.10 Interplanetary Magnetic Field	8
3 Background of Spectrum Estimation ...	10
3.1 Standing Waves and Modes	10
3.2 Nonradial Oscillations	11
3.3 Kernels of Interest	12
3.3.1 Dirichlet Kernel	12
3.3.2 Fejér Kernel	12
3.4 O Notation	13

3.5	Stationary Processes	13
3.6	Orthogonal Increment Processes	14
3.7	The Problem of Spectrum Estimation	16
3.8	Naive Solution to the Problem	17
3.9	Direct Estimates	19
3.10	Maximizing Concentration	21
3.11	Multi-taper Spectrum Estimate	22
3.12	Weiner Interpolation	26
	3.12.1 Pre-whitening	28
	3.12.2 The Central Chi-Squared Distribution	29
	3.12.3 The Non-Central Chi-Squared Distribution	30
	3.12.4 Fisher F-distribution	30
3.13	Hypothesis Testing	31
3.14	Harmonic Analysis	32
4	Pre-Analysis	35
4.1	Gap Filling	35
	4.1.1 Moving-Average Filter	37
	4.1.2 Linear Predictor	38
	4.1.3 Spectrum Smoother	39
	4.1.4 Autocovariance Sequences	40
	4.1.5 Further Work	40
4.2	Downsampling	41
4.3	Prewhitening	48
4.4	Conclusion	50
5	Analysis	52
5.1	What to look for?	52
5.2	The initial F-test	53
5.3	Sectioned F-tests	55
5.4	Inside the Bow Shock	64
	5.4.1 Post-Jupiter Approach	71
5.5	Comparing Models to Data	74
	5.5.1 Gudkova Model Comparison	75
6	Summary and Conclusions	78
6.1	Summary	78
6.2	Future Work	80
6.3	Conclusion	82

7 Appendix	83
7.1 Table in Full	83
Bibliography	88

List of Tables

4.1	Format of Original .TAB Files	37
5.1	F-test Results on 8 Sets, 4096-point FFT	56
5.2	F-test results on 8 sets, 8192-point FFT	57
5.3	F-test Results: Significant Frequencies from Pre-Bow-Shock Data	63
5.4	Voyager 2 Dates of Interest	64
5.5	F-test Results on Closest Approach Data	66
5.6	F-test Results: Significant Frequencies from Closest Approach	70
5.7	F-test Results: Significant Frequencies from Post-Approach	73
5.8	Results from Mosser <i>et al.</i> [27]: $l = 1, m = \pm 1$	74
5.9	Results from Mosser <i>et al.</i> [29]: $l = 2, m = \pm 1$	75
5.10	Results from Gudkova and Zharkov [19]: $l = 1, \dots, 10$	76
5.11	Significant Results from Gudkova and Zharkov [19]: $l = 1, \dots, 10$	77
7.1	F-test Results for Closest Approach (full)	83

List of Figures

4.1	Moving-Average Method for Gap-filling	42
4.2	Difference between Linear Interpolation and Moving-Average Methods	43
4.3	Smoother used on Interpolated Data	44
4.4	Data (black) and Linear Predictor (red)	44
4.5	Residual Data Series $x_{res}(\cdot)$	45
4.6	30:1 Lowpass Decimation Filter	45
4.7	Spectral Window	46
4.8	Comparison of Interpolation Methods	47
4.9	Cleaned Data: X-axis	48
4.10	Initial Spectral Estimate: X-axis	49
4.11	Time Series post-AR Filter	51
4.12	Estimated Spectrum Post-Prewhitening	51
5.1	Initial F-test (2,14 degrees-of-freedom)	54
5.2	F-test Results for Area around 4.06 mHz: Four Data Sets	60
5.3	F-test Results for Area around 1.19 mHz: Four Data Sets	62
5.4	Closest Approach	65
5.5	F-test for 4.06mHz around Closest Approach	68
5.6	Pre-Whitened Spectrum	71
5.7	Pre-Whitened Spectrum (2)	72

Chapter 1

Introduction

In this thesis we examine data obtained from the Voyager 2 project as it approached and departed from Jupiter in the summer of 1977. Specifically, we analyze the fluxgate magnetometer data. Voyager 2 carried 3 axial fluxgate magnetometers, each one sampling at a recorded 1.92 seconds. This data has been available for almost 30 years, and yet a detailed study of the spectrum has never been carried out.

Studies of Jupiter have been carried forth for many years. The first modern work which had an impact on these studies was the discovery of Gilbert and Backus [2] that the Earth's modes could be tracked and recorded. This logically led to helioseismic studies with interesting results first appearing in [8], and from there, to the foundational 1974 and 1976 papers of [44],[45]. With the theoretical basis set, a number of scientists, led primarily by Mosser and Schmider [29],[5] began experimental attempts to verify the theoretical modal structure of this planet.

Significant results were obtained in [29], [5], [6]. Currently, Mosser *et al.* are working on the funding and design of a new microsatellite named JOVIS that will be launched into Earth's orbit and will enable high-resolution imaging of Jupiter. They

hope that the results will give a clearer picture of the modal structure, enabling them to confirm or refine the current models.

Strangely, we have been unable to find any real research tying together the magnetic data from Ulysses, Voyager 1, and Voyager 2 with the modal structure of Jupiter. In 1996, D.J. Thomson presented a paper to the annual meeting of the American Geophysical Union concerning the Ulysses results, especially as they corresponded to the then-current discussion of whether or not the solar medium was turbulent. The short answer is: it is not. These results were made available to us as we began the thesis, and have proved valuable as a cross-check of results. The Voyager 2 data is cleaner, and of higher resolution than the Ulysses data, but the same features have been observed.

In our summary of literature, we fully review all previous studies done of Jupiter, with special emphasis on the theoretical models and their development to today's accepted theory. We consider the methods used, and briefly comment on the validity of their approaches.

We detail the theory behind the multitaper spectrum estimate, especially as it corresponds to time series. We detail the theory behind the harmonic frequency variance test (hereafter referred to as the F-test), as it proved to be the most valuable tool of all in this analysis. We also diverge into some discussion on gap-filling and filter design, as both were done as pre-analysis operations to the data set, to clean the data and reduce it to manageable size.

Chapter 2

Background on Jupiter Research

2.1 Early Work

One of the essential characteristics of any planet is its free oscillations. Measuring the periods of these oscillations allows the sounding of the interior of the planet of interest. This has been successfully executed on Earth, beginning in the late 1950s with the work of Gilbert and Backus [2], and was extended to helioseismic applications with the work of Gough, Christensen-Dalsgaard, Provost, Palle, and Turck-Chieze, among others. A suitable example of the development can be seen in [8]. In 1974 the concept was extended to Jupiter by Hubbard, Trubitsyn, and Zharkov [44] and continued by Vorontsov, Zharkov, and Lubimov [45] in 1976, leading to the first, albeit crude, theoretical models for the modal structure of the planet.

Initially, the assumption was made that Jupiter was a gaseous-liquid adiabatic body, and the models were constrained to what astronomical data was then available for the external characteristics. This work resulted in two tables, one listing a few of the lower order modes for $n = 1, \dots, 7$, and the second the rotational splitting for

the same [45]. It should be noted that these *free oscillations* are distinct from the short-period, high-degree oscillations confined to the Jovian waveguide [3], and do not depend in any way on the presence of the cavity.

2.2 Asymptotic Approximations

The problem of nonradial oscillations of stars (and by extension, planets) attracted a great deal of research attention through the latter half of the 20th century. Numerical methods allowed some precision to be obtained, but there were cases [18] of *resonance* between noncontiguous wave propagation zones in some models. This theoretical development pointed to the need for greater precision in the numerical analysis, aiming toward sufficient resolution to distinguish between the individual waves. The work of Tassoul [38] was primary in the advancements in this area.

Using asymptotic expansions for the eigenfunctions, modelists were able to distinguish between the various wave propagation zones, and new models soon resulted. The full details are well beyond the scope of this thesis.

2.3 An Additional Model

Playing off of the success of the helioseismic model, Bercovici and Schubert [3] proposed that acoustic waves were likely to be trapped below the tropopause of Jupiter. They additionally suggested that detection of these short-period oscillations would prove the validity of Jovian seismology as a tool for probing below the surface of the planet, just as it had been proven for Earth and the Sun. The oscillations would be of short-period and high-degree, and would be more readily observable using the

partial- or full-disc methods that are currently in use for solar observations.

2.4 The First Proposal

As the internal structure of Jupiter was as yet unproven (circa 1988), Mosser, Gautier, and Delache [4] presented a short paper in September of 1988. This presentation laid the groundwork for almost twenty years of experimental results for the Red Giant. In this presentation, they detailed the then-current status of the planetary model, and noted that the core mass estimate fluctuated by more than 50% (based on gravitational readings from Voyager 1 and Pioneer). As well, the first hint of the hydrogen-metallic boundary appeared, with a note that ‘*Another discontinuity appears in the jovian structure because of the possible existence of metallic hydrogen ... will induce a different propagation of the high-degree p -modes*’.

At this point, Jupiter’s rotation was unknown to any degree of certainty, the phase transitions were muddy at best, and there had been no observations of p -modes, not to mention g -modes. As well, it should be noted that at this point that full statistical examination of the results from Voyager 1 and Voyager 2 was merely a pipe-dream. In the words of Dr. David Thomson, ‘... *not even a pipe-dream, as the first statistical analysis of data of this sort wasn’t until 1995 ...*’.

2.5 Tentative First Observation

At the same time as the paper above was presented, work was being done on a more efficient instrument for study of the Doppler shift of a solar sodium D line, reflected from Jupiter, and observed through optical resonance spectrophotometry. Located in

Nice, the instrument was used for six nights of observations, with the experimental procedure detailed in [5]. The instrument was not sensitive to modes of degree higher than 2, but observed solar light being reflected at a level of approximately 3 bar. The results were somewhat equivocal, and a note was made at the end of the paper that a number of the possibly observed modes seemed to be obnoxiously spread, not separated by rotational frequency (28 uHz) or even twice that, but anywhere from 1 to 5 times the rotational. They concluded that the best way to analyze the data was likely to create a rigorous theoretical model, and then attempt to match the model to the data, acknowledging that modes can appear as \pm rotational, or even multiples thereof.

Several months later, there was a Paper II published by the same group in which the first experimental results were fully detailed [36]. In this paper, a number of low- n modes were observed, most especially $l = 1$ modes, at splitting precisely twice the Jovian rotational frequency. The conclusion was that the influence of the window function (due to a single ground-based observatory) is even worse for Jovian seismology than for helioseismology, and that further observations should be made from space.

2.6 Theory Catches Up with Observation

Further work continued on the study of Jupiter, with Mosser [28] examining the pressure mode oscillation spectrum; Mosser, Gautier and Kostjuk [29] examining the possibility of infrared heterodyne measurements; and Mosser *et al.* [5] using a Fourier transform spectrometer to expand on the work done in 1987 in Nice. The latter had some results consistent with the first observation, with a few scattered doublets for

low-order $l = 1, 2, 3$ modes appearing in the data. The window function that was used resulted in far too much bias to analyze the data any further.

Papers by Lee [24], Provost, Mosser and Berthomieu [34], and Gudkova and Zharkov [19] continued the development of the theoretical models of the Jovian core. Gudkova and Zharkov made an especially detailed examination of the free oscillations for several different models, and provided a great deal of data for checking our spectrum results.

2.7 Further Attempts

Mosser *et al.* attempted another observation of Jupiter in 1996 with results published in 2000 [6] using the Fourier transform spectrometer as an accelerometer. Results were mostly spurious due to instrument difficulty, although there was strong evidence in the data for a large splitting ν_0 at 142 ± 3 uHz, where ν_0 represents the characteristic frequency of the core rotation. The results also gave indication of a very small radius planetary core, developing from the value of ν_0 .

Cacciani *et al.* [1] repeated the search for global oscillations using a double-cell sodium filter, similar in form to the first work done by Mosser in the late 1980s. This team focused their instrument to a limited portion of Jupiter's surface, and found similar structures to the Mosser results, within the bounds of different instrumentation. No concrete results were obtained.

2.8 Radio Period Fixed

A short paper by Higgins, Carr, and Reyes [21] fixed the Jovian radio rotation period within 27 milliseconds, giving confirmation of the rotational frequency for splitting. Their result was a period of 35729.685 ± 0.0034 seconds, giving a rotational splitting frequency of 27.988 uHz.

2.9 Results since 1999

Since 1999, Mosser (who largely pioneered or guided the work) has been largely caught up with getting a new instrument developed and launched. Named JOVIS, it is a microsatellite that is being launched for the express purpose of studying Jupiter, and should lead to exciting results. Research has somewhat stalled until the instrument can be launched and meaningful results are obtained [26].

Some small results have been obtained in the theoretical realm, mostly with respect to the troposphere and cloud structure of Jupiter. No major papers have been found detailing new models or theories for the free or acoustic modes of the planet.

2.10 Interplanetary Magnetic Field

A paper was published in 1995 by Thomson, McLennan, and Lanzerotti [43] which concluded that energetic particle fluxes in the interplanetary medium carried signatures of discrete modes. This was followed up with a paper in 2001 which extended the study using 1-hour average interplanetary magnetic field data acquired by the Ulysses magnetometer [42]. The conclusion was that the interplanetary medium is

not a totally chaotic medium. This research gives justification for the techniques used in this thesis for study of Jupiter, as we are detecting Jovian influence in the magnetic field readings *around* Jupiter, at distances beyond that previously thought possible.

Chapter 3

Background of Spectrum

Estimation and Physical Theory

3.1 Standing Waves and Modes

The term *standing wave* is often applied to a resonant mode of a vibrating object, created by constructive interference of multiple waves. In the context of a rotating stellar body (such as Jupiter), the vibrating object is the planet itself, and the modes are the resonances created by restorative pressure and gravity waves inside the planet. As the planet rotates, there is movement of the fluid layers, with gravity and pressure acting both in opposition and support of the rotational forces. In a similar way to pressure modes in a hollow tube filled with air, there are modal structures within the surface of a fluid sphere, which is a (mostly) accurate model for the great gas giant.

3.2 Nonradial Oscillations

Nonradial Oscillations refers in the context of this thesis to internal pressure and gravity waves of Jupiter, and their interaction with the surface of the planet. We refer to a restorative pressure wave in terms of its *p-modes*, and similarly for gravity, *g-modes*. As Jupiter rotates, pressure and gravity waves act upon the interior of the planet, restoring and opposing the motion of the various subsurface layers. Nonradial stellar pulsations are characterized by their frequency and three quantum numbers. The radial dependence of the variations is specified by the radial order n which equals the number of nodes between the center and surface of the stellar body. The angular dependence of the variations is described by spherical harmonics and is specified by the azimuthal order m , where $2|m|$ specifies the number of nodes in longitude, and the nonradial degree l , where $l - |m|$ specifies the number of nodal lines in planes parallel to the equator. The azimuthal order may take on the values $m = -l, -l + 1, \dots, l$.

These oscillations are visible upon the surface of Jupiter when it is observed through an optical resonance spectrophotometry technique, essentially measuring the Doppler shift in a Sodium-D line as the surface of Jupiter moves. It is currently an open topic as to the precise interaction between surface movements (as measured by Mosser et al. in [5]) and the magnetic field of surrounding space. Some theoretical models explain a strong relation between the two, indicating that the movement of the surface transmits a frozen image of the internal magnetic field to the fields surrounding the planet. In this case, we hope to observe the influences of the internal restoring modes on the magnetic fields, and in so doing, confirm the theoretical models that set out frequency estimates for the low-order *p*- and *g*-modes.

3.3 Kernels of Interest

In the development of the multitaper spectrum estimate, we will refer several times to the Dirichlet and Fejér kernels. We give here a small background of both.

3.3.1 Dirichlet Kernel

The Dirichlet kernel is the family of functions

$$D_n(x) = \sum_{k=-n}^n e^{ikx} = 1 + 2 \sum_{k=1}^n \cos(kx) = \frac{\sin \frac{(2n+1)x}{2}}{\sin \frac{x}{2}} \quad (3.1)$$

and arises in relation to the study of Fourier series. The convolution of $D_n(x)$ with any 2π -periodic function f is the n^{th} -degree Fourier series approximation of f .

3.3.2 Fejér Kernel

The Fejér kernel is defined as

$$F_n(x) = \frac{1}{n} \sum_{k=0}^{n-1} D_k(x) \quad (3.2)$$

which can be written in closed-form as

$$F_n(x) = \frac{1}{n} \left(\frac{\sin \frac{nx}{2}}{\sin \frac{x}{2}} \right)^2 \quad (3.3)$$

and results from the summation of Fourier series.

3.4 O Notation

For two functions $f(\cdot), g(\cdot)$ we say that $f(\cdot)$ is of **order- g** , denoted $f = \mathbf{O}(g)$ if, for an index set T , $\exists N \in T$ such that $\forall n > N$, we have that $\left| \frac{f(n)}{g(n)} \right|$ is bounded.

3.5 Stationary Processes

The primary class of models for spectral analysis is that of the stationary stochastic process. The precise definition depends on the concept of a random variable acting as a map from the sample space of possible outcomes of a random experiment to some Euclidean space [30, p.31]. Formally:

Definition. *A stochastic (random) process is a family of random variables $\{X_t\}_{t \in T}$ indexed by a parameter t , where t belongs to some index set T .*

We will assume in all further usage of this definition that T is a discrete set, as all analysis being done in this thesis is done on digitally sampled data.

In spectral analysis, we restrict ourselves largely to the case of stationary processes from the larger family of random processes, where stationary processes are those that have certain statistical properties invariant with respect to time [30, p.35]. There are two types of stationarity: *complete (or strong) stationarity* and *weakly (or second-order) stationary*. We define both as follows.

Definition. *A random process $\{X_t\}$ is said to be **strongly stationary** if for all $\{t_1, \dots, t_m\} \subset T$; $\tau, m \in \mathbf{Z}$, we have*

$$F_{t_1, \dots, t_m}(a_1, \dots, a_m) = F_{t_1 + \tau, \dots, t_m + \tau}(a_1, \dots, a_m)$$

where F_α is the joint cumulative probability density function of the set α .

and

Definition. A random process $\{X_t\}$ is said to be **weakly stationary** if for all $\{t_1, \dots, t_m\} \subset T$, $\tau, m \in \mathbf{Z}$ we have all joint moments of orders 1 and 2 of X_{t_1}, \dots, X_{t_m} as finite and equal to the corresponding joint moments of $X_{t_1+\tau}, \dots, X_{t_m+\tau}$.

Quite simply, weak stationarity implies that the mean and variance of our process $\{X_t\}$ are constant with respect to t .

An interesting corollary of this gives that the covariance between X_{t_1} and X_{t_2} is also a function of the absolute difference $|t_2 - t_1|$.

3.6 Orthogonal Increment Processes

There is a spectral representation theorem for stationary processes known as the Cramér (or spectral) representation [40], [30, p.127]. This theorem allows us to relate the spectrum of a stationary process directly to a representation for the process. The representation is based upon the concept of an orthogonal increment process, which defines the probabilistic structure of the process. Our definition is due to Percival and Walden [30]. Begin by defining a complex-valued stochastic process:

$$Z(f) = \sum_{j=0}^l D_j e^{i\Phi_j}, \quad f_l < f \leq f_{l+1} \text{ with } l = 0, \dots, L \quad (3.4)$$

with $f_{L+1} = \frac{1}{2}$ and D_j real-valued constants, obtained from a real-valued discrete harmonic process. Also define $Z(0) = 0$. Now, we define

$$dZ(f) = \begin{cases} Z(f + df) - Z(f) & 0 \leq f < \frac{1}{2} \\ 0 & f = \frac{1}{2} \\ dZ^*(-f) & -\frac{1}{2} < f < 0 \end{cases} \quad (3.5)$$

where df is a small positive change so $0 < f + df < \frac{1}{2}$, for $0 < f < \frac{1}{2}$. It follows that $\mathbf{E}\{dZ(f)\} = 0$ for all f (with \mathbf{E} the standard expectation operator), and from this it can be shown that $dZ(f)$ and $dZ(f')$ are uncorrelated. The process $\{Z(f)\}$ is said to have *orthogonal increments* and is itself called an *orthogonal process*.

Using this definition, a few steps will suffice to show an outline of the derivation of the formal spectrum of the process. Take $g(\cdot)$ a continuous function on the interval $[-\frac{1}{2}, \frac{1}{2}]$ and define $H(\cdot)$ as a step function, with jumps at indices $\{a_i\}_{i \in [1, N]}$, where $-\frac{1}{2} < a_1 < a_2 < \dots < a_N < \frac{1}{2}$, with steps defined as the set $\{b_i\}_{i \in [1, N]}$.

From this, using the standard definition of the Riemann-Stieltjes integral, we have

$$\int_{-\frac{1}{2}}^{\frac{1}{2}} g(f) dH(f) = \sum_{j=1}^N g(a_j) b_j \quad (3.6)$$

and letting $g(f) = e^{i2\pi ft}$, and $H(f) = Z(f)$, we rewrite

$$X_t = \int_{-\frac{1}{2}}^{\frac{1}{2}} e^{i2\pi ft} dZ(f) \quad (3.7)$$

which is the *spectral representation* of the stationary process $\{X_t\}$. The equality cannot be justified except through rigorous proof, and the reader is directed to Priestly [33].

Both Percival and Walden [30] and Priestly [33] extend this definition with a note

that the properties of $\{Z(f)\}$ imply that for all frequencies f_1, f_2 in $[-\frac{1}{2}, \frac{1}{2}]$ with $f_1 \neq f_2$, $\mathbf{E}\{dZ(f_1)dZ^*(f_2)\} = 0$. Brockwell and Davis [11] continues the discussion with a more in-depth analysis of the stochastic integral in (3.7), but the details are beyond the scope of this thesis, and add little to the discussion beyond sheer curiosity.

3.7 The Problem of Spectrum Estimation

Given the discussion on orthogonal increment processes, and the definition of the *spectral representation*, we logically would like to extend the discussion to the actual steps needed to define as nearly a true (in the sense of unbiased) estimate of the spectrum of a stationary process as possible. Thomson [40] presents the problem as follows:

The measure $dZ(f)$ used for the orthogonal increments has (for a zero-mean process)

$$\mathbf{E}\{dZ(f)\} = 0 \quad (3.8)$$

and its second moment (the *spectrum* $S(f)$) defined as

$$S(f)df = \mathbf{E}\{|dZ(f)|^2\} \quad (3.9)$$

which presents the problem of how to estimate the moments of $dZ(f)$.

Assuming we have a stationary stochastic process $x(t)$, where t is taken as discrete of rate one, we can define the Fourier transform as

$$X(f) = \sum_{t=0}^{N-1} x(t)e^{-i2\pi ft} \quad -\frac{1}{2} \leq f \leq \frac{1}{2}. \quad (3.10)$$

We transform this into time-centered form

$$X(f) = \sum_{t=0}^{N-1} e^{-2i\pi f[\frac{t-(N-1)}{2}]} x(t) \quad (3.11)$$

and using the Cramér spectral representation of the previous section as a substitution for $x(t)$ into (3.11), we arrive at

$$X(f) = \int_{-\frac{1}{2}}^{\frac{1}{2}} \sum_{t=0}^{N-1} e^{i2\pi(\nu-f)[t-\frac{(N-1)}{2}]} dZ(\nu) \quad (3.12)$$

which, upon recognition of the summation as the Dirichlet kernel (see Section 3.3)

$$\frac{\sin N\pi(f - \nu)}{\sin \pi(f - \nu)} = \sum_{t=0}^{N-1} e^{i2\pi(\nu-f)[t-\frac{N-1}{2}]} \quad (3.13)$$

we write

$$X(f) = \int_{-\frac{1}{2}}^{\frac{1}{2}} \frac{\sin N\pi(f - \nu)}{\sin \pi(f - \nu)} dZ(\nu) \quad (3.14)$$

which Thomson [40] considers to be the basic equation of spectrum estimation. This equation is (again Thomson) a convolution that can be interpreted as a *smearing* of the true $dZ(f)$, where the smearing is a consequence of using a *finite* Fourier transform.

The problem then becomes finding an approximate solution to (3.14).

3.8 Naive Solution to the Problem

The most basic attempt at an estimate of the spectrum is to simply use the squared Fourier transform, known as the *periodogram*¹. Assuming we begin with a sample,

¹We will use the word *periodogram* to refer to a direct spectral estimate with spectral window $a(t) = 1$, and refer to any estimate with $a(t) \neq 1$ as a *direct estimate*, see 3.9

$\{x(t)\}$, where $t = 0, \dots, N - 1$, with the observations being taken from a stationary process $\{X(t)\}_{t \in T}$, we have the estimate

$$\widehat{S}(f) = \frac{1}{N} \left| \sum_{t=0}^{N-1} x(t) e^{-i2\pi ft} \right|^2. \quad (3.15)$$

Following the format of Percival and Walden [30, p.197-8], if our estimate $\widehat{S}(f)$ were ideal, we would have that:

1. $\mathbf{E}[\widehat{S}(f)] \approx S(f)$ for all f .
2. $\mathbf{var} [\widehat{S}(f)] \rightarrow 0$ as $N \rightarrow \infty$.
3. $\mathbf{cov} [\widehat{S}(f'), \widehat{S}(f)] \approx 0$ for $f' \neq f$.

For a stationary process with a continuous spectrum, the periodogram is asymptotically unbiased. In short, as N grows asymptotically, we have that the first property above holds. However, there is no real indication as to when this will occur in terms of N , and as Thomson [40] states, in a particular periodogram computed for the WT4 waveguide project from over 1.2 million samples, the periodogram remained too badly biased to be useful.

There are some stationary processes (again, [30]) for which the bias in the periodogram converges for small N . Brillinger details a regularity condition for a stationary process $\{X_t\}$, namely

$$\sum_{\tau=-\infty}^{\infty} |\tau S_{\tau}| < \infty \quad (3.16)$$

for S_{τ} the spectral representation of X_t , which then implies that

$$E[\widehat{S}(f)] = S(f) + \mathbf{O}\left(\frac{1}{N}\right) \quad (3.17)$$

where the \mathbf{O} operator has properties as outlined in Section 3.4.

When the condition above is true, the bias in the periodogram decreases at the rate of $\frac{1}{N}$, but it should be noted that this says absolutely nothing about **magnitude** of the bias, merely its rate of convergence.

Considering the variance of the periodogram, we have the condensed result (courtesy of Priestley [33]) that says that for an assumed Gaussian process $\{X_t\}$, and considering the periodogram only on the Fourier frequencies,

$$\mathbf{var}[\widehat{S}(f)] = \begin{cases} 4(\mathbf{var}[X_t]^2) & f \neq 0, \pm 1, 2 \\ 8(\mathbf{var}[X_t]^2) & f = 0, \pm 1, 2 \end{cases} \quad (3.18)$$

which clearly shows that the periodogram could never be consistent, as variance will never converge to 0.

Thus the periodogram is essentially biased, inconsistent, and furthermore, for a stationary process with a continuous spectrum, the periodogram of a sample of this process does not even converge to a random variable as $N \rightarrow \infty$, much less the spectrum (a result due to Grenander, obtained from [33]).

3.9 Direct Estimates

Logically, given that the periodogram is biased and inconsistent, we would like to directly attack the issue of bias. To do this, a sequence of estimates were derived based around the fundamental idea of a *taper*. The idea is to directly reduce the size of the sidelobes of the Fejér kernel (detailed in 3.3), thus reducing the bias in our estimate $\widehat{S}(f)$ that came from the leakage of power from one section of the spectrum to another.

We write our *direct estimate* of the spectrum (definition due to [30]):

$$\widehat{S}^{(d)}(f) = \left| \sum_{t=0}^{N-1} a(t)X(t)e^{-i2\pi ft} \right|^2. \quad (3.19)$$

First, recall that to ensure total power is preserved, we must ensure that $\{a(t)\}$ is normalized, *i.e.*,

$$\sum_{t=0}^{N-1} |a(t)|^2 = 1. \quad (3.20)$$

We then must examine the frequency-domain characteristics of the taper, which we approach by first Fourier transforming the taper:

$$A(f) = \sum_{t=0}^{N-1} a(t)e^{-i2\pi ft} \quad (3.21)$$

where $|A(f)|^2$ is commonly referred to as the *spectral window*. In most conventional tapers, $A(f)$ consists of a very broad main lobe, with numerous sidelobes which consist of drops of anywhere from 10 to 100 dB.

If we rewrite the above estimate as a convolution of the spectral window and the true spectrum,

$$\mathbf{E} \left[\widehat{S}^{(d)}(f) \right] = \int_{-\frac{1}{2}}^{\frac{1}{2}} |A(f)|^2 S(f - f') df' \quad (3.22)$$

and we can see that again, as in (3.14), there is *smearing* of the true spectrum. We desire a taper with low amplitudes for large $|f - f'|$ in order to ensure our estimate $\widehat{S}^{(d)}(f)$ is based primarily on **local** information, *i.e.*, information close to our frequency of interest f .

Ideally, we wish to chose a spectral window that has much smaller sidelobes than that of the Fejér kernel, in order to reduce the effects of global bias. Percival and Walden give a great deal of detail concerning the individual characteristics of some

choices of tapers, which are interesting in their own right, although provide little to the discussion here.

3.10 Maximizing Concentration

Given that we have chosen to taper our data (despite the somewhat interesting arguments against *tapering* with the data [30, p. 216]), we wish to minimize leakage (in our spectrum estimate) at frequency f from frequencies $f' \neq f$. There is little point being concerned with frequencies that are within $\frac{1}{N}$ of f , as we cannot realistically discern between such frequencies anyway (given a record length of N). Thus, if we choose a bandwidth W such that $\frac{1}{N} < W < \frac{1}{2}$, we can determine the fraction of energy from the spectral window in the band $(-W, W)$. This is simply given by:

$$\lambda(N, W) = \frac{\int_{-W}^W |A(f)|^2 df}{\int_{-\frac{1}{2}}^{\frac{1}{2}} |A(f)|^2 df} \quad (3.23)$$

where $\lambda(N, W)$ is a unitless measure of concentration. Obviously $0 < \lambda(N, W) < 1$, by our definition of W . We would like to ideally maximize $\lambda(N, W)$, so as to obtain maximal information through use of our taper.

To maximize $\lambda(N, W)$, without a detailed explanation, we take the gradient of λ with respect to a vector consisting of the elements of the taper, and setting it to zero, obtain a matrix eigenvalue problem where entries in the matrix are of the form

$$\frac{\sin 2\pi W(t - t')}{\pi(t - t')} \quad (3.24)$$

for $t, t' = 0, 1, \dots, N - 1$. It has been shown [37], [40] that the discrete prolate spheroidal wave sequences (referred to from here on as the Slepian sequences) and

their eigenvalues are actually the solution to this eigenvalue problem, and, as an interesting solution, have the greatest fractional energy concentration in $(-W, W)$. This makes the zeroth-order eigenvalue the ideal choice as a taper for bandwidth $(-W, W)$.

Additionally, the first $2NW - 1$ solutions to this equation all have eigenvalues close to 1. Recall that this is equivalent to the measure $\lambda(N, W)$ of spectral concentration, and their eigenvectors are equivalently *good* choices as tapers. This gives us a family of tapers with good spectral leakage properties, which is exactly how the multitaper spectrum estimate uses them.

3.11 Multi-taper Spectrum Estimate

We have discussed how the first $2NW - 1$ solutions to the matrix eigenvalue equation mentioned above are good choices as tapers. Given that we have this excellent family of tapers, the question becomes how to use them effectively to obtain estimates of the spectrum. First, we will list a few of the properties, and define our notation for the remainder of the thesis.

We will follow the notation that was used in [40], as it has the benefit of carrying all dependencies along with each step. The eigenfunctions will be denoted by:

$$U_k(N, W : f) \tag{3.25}$$

and are the discrete prolate spheroidal wave functions (DPSWF), and with each is associated its eigenvalue:

$$\lambda_k(N, W) \approx 1 - \frac{\sqrt{2\pi}}{k!} (8N\pi W)^{k+\frac{1}{2}} e^{-2N\pi W} \tag{3.26}$$

These eigenfunctions will be used as tapers in the Multitaper Spectrum Estimate. The Fourier transforms of the sequences are the discrete prolate spheroidal wave functions (DPSWF), or Slepian functions, and are the spectral windows of the aforementioned tapers:

$$v_n^{(k)}(N, W) = \frac{1}{\epsilon_k \lambda_k(N, W)} \int_{-W}^W U_k(N, W; f) e^{-i2\pi f[n - \frac{N-1}{2}]} df \quad (3.27)$$

and are valid for $k = 0, 1, \dots, N-1$ and all n . Note that ϵ_k is a scale factor, simplifying the writing of the equation.

The objective will be to estimate the spectrum $S(f)$ by using the first K Slepian sequences to obtain K eigenestimates [40]. We begin by defining the *eigencoefficients*

$$y_k(f) = \sum_{n=0}^{N-1} x(n) \frac{v_n^{(k)}(N, W)}{\epsilon_k} e^{-i2\pi f[n - \frac{N-1}{2}]} \quad (3.28)$$

which is the discrete Fourier transform of the data, using the k^{th} Slepian sequence as a data taper. Note that ϵ_k is alternatively 1 or i depending on the even/odd nature of the Slepian sequence. From these eigencoefficients we form K eigenspectra

$$\widehat{S}_k(f) = |y_k(f)|^2 \quad (3.29)$$

from which we hope to generate some form of averaged spectrum.

Percival and Walden [30] detail two different algorithms for forming a final multitaper estimate. Their first example is the same as the one explained in [40], namely a simple average over all K eigenestimates, while the second, also in [40], is an adaptive weighted average.

The first is simple to write, namely:

$$\bar{S}(f) = \frac{1}{K} \sum_{k=1}^K \widehat{S}_k(f) \quad (3.30)$$

since for $K < 2NW - 1$, we have the eigenvalues $\lambda_k(N, W) \approx 1$, such that

$$\bar{S}(f) = \frac{1}{\sum_{k=1}^K \lambda_k} \sum_{k=1}^K \lambda_k \hat{S}_k(f) \approx \frac{1}{K} \sum_{k=1}^K \hat{S}_k(f) \quad (3.31)$$

However, since the idea of taking an average over K eigenspectra is to reduce the variance in the spectral estimate, we must ask if the mean spectrum is truly ideal.

The spectral leakage properties of the initial $\hat{S}_0(f)$ eigenspectrum are very good, but for each increment in k , the leakage characteristics degrade in quality. For further information on this, along with some clarifying images, see [30, p.335-339]. Clearly, if we were to limit K to $K = 1$, we would obtain the best possible leakage characteristics from our mean spectrum, *i.e.*,

$$\hat{S}(f) = |y_0|^2 \quad (3.32)$$

This is where the balancing game comes in. For each increment in K , we increase the spectral leakage, but decrease the variance of the spectral estimate. The balancing point is a delicate one, and is typically chosen as $K = 2NW - 2$ or $K = 2NW - 1$, using the maximum number of available *good* spectral windows, *i.e.*, eigenestimates for eigenvalues close to 1.

The second method mentioned above, namely that of adaptive weighting, was originally published by Thomson [40]. He encourages his readers to consider the following four points when considering why to use more than a single window in an estimate:

- The eigencefficients are almost uncorrelated for locally *reasonably white* spectra, and thus the estimate has approximately $2K$ degrees of freedom.
- There is no decrease in resolution.

- The variance efficiency of the estimate is good, typically better than 80%.
- The effective spectral window associated with the estimate approaches ideal with the inclusion of the other tapers.

As in the development in [40], we must consider the DPSWF Fourier-Bessel coefficients of the orthogonal increment process dZ in the passband $(f - W, f + W)$:

$$Z_k(f) = \frac{1}{\sqrt{\lambda_k(N, W)}} \int_{-W}^W U_k(N, W; \nu) dZ(f + \nu) \quad (3.33)$$

While these $Z_k(f)$ are unobservable, they are of significant interest, as they are the coefficients that would be obtained if the entire original sequence were passed through an ideal bandpass filter **before** being truncated to a finite sample size.

If we were to estimate these coefficients by expanding the Fourier transform of our data sample, $\{x(t)\}$, over the same passband $(f - W, f + W)$ using the same set of basis functions:

$$y_k(f) = \frac{1}{\lambda_k(N, W)} \int_{-W}^W U_k(N, W; \nu) X(f + \nu) d\nu \quad (3.34)$$

we could then weigh these estimates using a sequence of weight functions $d_k(f)$ and minimize the mean-square error between the estimates and the $Z_k(f)$ mentioned above.

Thomson shows that the weights that should be used are

$$d_k(f) = \frac{\sqrt{\lambda_k} S(f)}{\lambda_k S(f) + (1 - \lambda_k) \sigma^2} \quad (3.35)$$

with σ^2 taken as the variance of our sample $\{x(t)\}$. Of course, we do not **know** the spectrum $S(f)$, so it will be necessary to form an iterative algorithm. In [40], Thomson suggests forming an initial estimate (for example, the mean estimate of

$\widehat{S}_0(f)$ and $\widehat{S}_1(f)$) and using this iteratively to find weights. He claims [40, p.1065] that convergence to a 5% differential is as rapid as 2 to 3 iterations.

There are additional methods that can be used for forming spectral estimates from the eigenspectra. In [39] Thomson notes that there is a method called *coherent sidelobe subtraction* which is the best way to manage the bias properties, but is numerically delicate. Thus the most common method presented in the literature is that of the adaptive weighting described above.

3.12 Wiener Interpolation

In time series analysis, we are often presented with an incomplete (real-world) data set, often recorded digitally, on some discrete mesh. We know the value of the ensemble function at a set of points $\{x_i\}_{i \in \mathbf{N}}$ for \mathbf{N} an index set. Unfortunately, due to instrument error, noise, or recording error (often human in origin, although here, the clipping of an occasional bit as the data is transmitted over 5 AU), we may never have our index set \mathbf{N} fully complete. Accordingly, we would like to be able to estimate our ensemble function $f(x)$ for some arbitrary x .

If the x is located between the minimum and maximum values recorded by the instrument, the problem is called *interpolation*; if x is outside this range, the problem is called *extrapolation* [16].

Weiner interpolation is a method of interpolating data that differs from the simple methods of polynomial interpolation in that it is based on the expected correlation of the data, rather than on the data points themselves [46]. The actual interpolation is quite simple, and is based largely on a single matrix equation. Advantages include:

- Data inputs can be arbitrarily spaced.

- The algorithm comes with a built-in confidence level for each interpolated point.
- The algorithm is optimal in that it minimizes the expected squared error.

The derivation is rather simple. Given a stationary random process, $\{x(t)\}$, the squared error of a linear estimator will be minimized when

$$\mathbf{E}\{(x - \hat{x})x_k\} = 0 \quad \forall k \quad (3.36)$$

and given that we chose our \hat{x} as some weighted sum

$$\hat{x} = \sum a_j x_j \quad (3.37)$$

we have

$$0 = \mathbf{E}\{(x - \sum a_j x_j)x_k\} = \mathbf{E}\{x x_k - \sum a_j x_j x_k\} \quad (3.38)$$

and we know that $\mathbf{E}\{x_j x_k\} = \mathbf{Corr}[t_j - t_k]$ so

$$\mathbf{Corr}[t - t_k] = \sum a_j \mathbf{Corr}[t_j - t_k] \quad (3.39)$$

or, writing the correlations in a matrix \mathbf{C} indexed by j, k , with the a_i as a column vector \mathbf{a} , with the $t - t_k$ correlations as another column vector \mathbf{c} :

$$\mathbf{c} = \mathbf{C}\mathbf{a} \quad (3.40)$$

We then form our estimate as

$$\hat{x} = \mathbf{a}^T \mathbf{C}^{-1} \mathbf{c} \quad (3.41)$$

3.12.1 Pre-whitening

We described in Section 3.9 methods that can be used to reduce the bias in the spectrum estimates that we perform. One further way of reducing bias effects is to lower the dynamic range of the spectrum through a filtering process known as *prewhitening* [32], yet another Tukey-ism (referring to John Tukey, of Bell Labs, who coined many scientific and technical terms that are in use today, such as *byte* and *bit*). Thomson [41] describes an adaptive process for developing such a filter.

We begin by cleaning the data. This involves interpolating (through varying methods) missing data points, clipping **obvious** outliers, removing known trends, and typically removing the average. We denote this cleaned data set by $\{x(t)\}_{t=1,\dots,N}$. We then compute a pilot spectrum estimate, typically done with a multitaper spectrum estimate, at a low resolution. We denote this estimate by $\tilde{S}(f)$.

We then transform this spectrum estimate into the lag- k autocorrelations, and using those, estimate a low-order autoregressive (AR-P) model. The order will vary, but should be chosen to reduce the overall range of the spectrum estimate to several decades. That is, we desire the ratio of the maximum-to-minimum to be less than 100 (in the whitened series).

We then filter the data using the AR-model

$$y(t) = x(t) - \sum_{j=1}^P a_j x(t-j)$$

and compute another spectrum estimate. Again, we use the multitaper estimate, and this time, we desire high frequency resolution. Denote this estimate by $\hat{S}(f)$, and

then correct for the filtering operation by *post-colouring* (another Tukey-ism)

$$\widehat{S}_{pc}(f) = \frac{\widehat{S}(f)}{\left|1 - \sum_{j=1}^P a_j e^{-i2\pi f k_j}\right|^2} .$$

Percival and Walden [30] note that the chief difference between this approach and that of a purely parametric approach, *i.e.* estimating parameters from the data, and determining a model, is that we do not regard the prediction errors $\{y(t)\}$ as white noise, but use a nonparametric approach to estimate their spectral density function. Additionally, they note that this technique largely makes sense in cases where there is large dynamic range for the spectral density function, which is exactly a situation where tapering is needed anyway. Here it has the effect that adaptive weight usually gives all 2NW tapers.

3.12.2 The Central Chi-Squared Distribution

The χ^2 distribution is a continuous probability distribution, concentrated on $(0, \infty)$, with probability density function

$$p(x) = \frac{1}{2^{n/2} \Gamma(\frac{n}{2})} e^{-x/2} x^{n/2-1}$$

with $\Gamma(\alpha)$ the gamma function, and the parameter n is known as the *degrees-of-freedom* or *dof*.

If we have $\{x_1, \dots, x_\nu\}$ independent, zero-mean, unit-variance Gaussian random variables, *i.e.* $x_j \sim N(0, 1)$, then the sum of the squares of these random variables is distributed as a central chi-squared distribution with ν degrees of freedom.

This comes into play in our examination, as at frequencies distant from periodic signals, most direct estimates (on which the multitaper is based) have χ_2^2 distributions,

where χ_2^2 is a chi-squared distribution with 2 *dof*. It should be noted that the sample mean for a chi-squared random variate is an unbiased estimate of the process mean.

3.12.3 The Non-Central Chi-Squared Distribution

If, instead, our ν random variates are normally distributed with means μ_i , the sum of their squares

$$z = \sum_{j=1}^{\nu} x_j^2$$

will have a non-central chi-squared distribution with non-centrality parameter,

$$\lambda = \sum_{j=1}^{\nu} \mu_j^2.$$

The non-central chi-squared distribution occurs commonly in spectrum estimation problems, and often can be an appropriate model for a badly biased estimate.

This distribution is important as the spectrum directly surrounding modes (the subject of this thesis) as they are largely deterministic.

3.12.4 Fisher F-distribution

The F-distribution arises naturally as a transformation from the beta distribution, which is detailed in [17]. It appears most often in applied statistics as an outcome to the following theorem:

If x_1 and x_2 are independent random variates, distributed as chi-square with ν_1 degrees of freedom, then

$$y = \frac{x_1/\nu_1}{x_2/\nu_2}$$

has an F-distribution with ν_1 and ν_2 degrees of freedom.

In our harmonic frequency variance test, we are presented with a test statistic that is the ratio of two chi-squared random variates. Between modes we will be presented with two central chi-squared distributions; near modes we will be presented with two non-central; and at modes we will have one each of central and non-central chi-squared distributions. If we denote our two chi-squared variates as

$$\chi_{\nu_1}^2(\lambda_1), \chi_{\nu_2}^2(\lambda_2)$$

then this distribution can be written as

$$F''_{\nu_1, \nu_2}(\lambda_1, \lambda_2) = \frac{\nu_2 \chi_{\nu_1}^2(\lambda_1)}{\nu_1 \chi_{\nu_2}^2(\lambda_2)}.$$

3.13 Hypothesis Testing

In this thesis we are testing for the presence of discrete modes in magnetic field data. This is, essentially, a form of hypothesis test. As a null hypothesis we will assume that the spectrum is *smooth*. This assumption is born up by early work that assumed turbulence in the interplanetary magnetic field and planetary magnetosphere, since such turbulence would destroy periodic components, resulting in a smooth spectrum. In such a case, the estimates of spectra will have a central χ^2 distribution, and similarly, the eigencoefficients will be approximately independent complex Gaussian random variates.

The alternative hypothesis is that discrete modes exist, and, at these frequencies, the eigencoefficients will have systematic non-zero means that can be detected by an F-test. Similarly, at these modal frequencies, spectrum estimates will have a non-central χ^2 distribution.

We will be testing for the failure of our null hypothesis of a smooth spectrum using harmonic analysis, as detailed in the next section.

3.14 Harmonic Analysis

Harmonic analysis is used in the context of this paper in the sense used by Thomson in [40], that is, as a study of mixed spectra ¹ in an attempt to detect lines and their structure. It should be noted that the problem presented here is in form similar to that of spectrum analysis, in that we are studying the orthogonal increment process $dZ(\nu)$, but is different in that we are interested here in the *first* moment of $dZ(\nu)$, rather than the second and higher.

We describe our process (assumed to be formed of line components plus a stationary random process) as having a non-zero mean function, which, in terms of the spectral representation, can be written:

$$\mathbf{E}\{dZ(f)\} = \sum \mu_m \delta(f - f_m) \quad (3.42)$$

rather than the usual

$$\mathbf{E}\{dZ(f)\} = 0 \quad (3.43)$$

In [40], Thomson makes the assumption that we have one simple line component at frequency f_0 , and develops the theory around that case. Since the test is easily extended to the case of multiple lines, we will follow this procedure and detail the case for one line.

Given one simple line component at frequency f_0 , we will have a non-zero expected

¹*Mixed Spectra* is used here to mean a case where line components are embedded in a background continuum that is a real-valued white-noise process with zero-mean [40], [30].

value

$$\mathbf{E}\{y_k(f)\} = \mu U_k(N, W; f - f_0) \quad (3.44)$$

and if we extend this with the assumption that the background spectrum at frequency $f = f_0$ is locally white, we have the result (again [40]) that

$$\mathbf{cov}[y_k(f), y_j^*(f)] \approx S(f)\delta_{j,k} \quad (3.45)$$

with $S(f)$ representing the continuous background spectrum, and $S(f)$ does **not** contain the power from the line component at f_0 .

Thomson details two methods for estimating μ : point regression at f_0 and integral regression in the neighbourhood of f_0 . In the former, and more common, case, we use data at f_0 and have

$$\mathbf{E}\{y_k(f_0)\} = \mu U_k(N, W; 0) \quad (3.46)$$

and using regression methods such as those detailed in [25]:

$$\hat{\mu}(f) = \frac{\sum_{k=0}^{K-1} U_k(0)y_k(f)}{\sum_{k=0}^{K-1} U_k^2(0)}. \quad (3.47)$$

Now, replacing $U_k(N, W; 0)$ with its Fourier-transform representation (3.28) and recognizing that the eigencoefficients are combined linearly, we have

$$\hat{\mu}(f) = \sum_{n=0}^{N-1} h_n(N, W)x(n)e^{-i2\pi f[n-\frac{N-1}{2}]} \quad (3.48)$$

with the data window $h_n(N, W)$ given as

$$h_n(N, W) = \frac{\sum_{k=0}^{K-1} U_k(0)\nu_n^{(k)}(N, W)}{\sum_{k=0}^{K-1} U_k^2(0)}. \quad (3.49)$$

The variance of the estimated mean then depends on the continuous part of the

spectrum local to the line component at $f = f_0$, *i.e.*,

$$\mathbf{var}[\hat{\mu}(f)] = \frac{S(f)}{\sum_{k=0}^{K-1} U_k^2(0)} \quad (3.50)$$

which can be approximated as $\frac{S(f)}{N}$. If we then subtract the estimate of the mean from the eigencoefficient, we have an estimate of the continuous background spectrum, which we can compare with the power contained in the line component. This results in a F-test (with 2 and $2K - 2$ *dof*) for the significance of the estimated line component [10]. The test can be written as

$$F(f) = \frac{(K - 1) |\hat{\mu}^2|^2 \sum_{k=0}^{K-1} U_k(N, W; 0)^2}{\sum_{k=0}^{K-1} |y_k(f) - \hat{\mu}(f) U_k(N, W; 0)|^2}. \quad (3.51)$$

It should be noted that in practice, a F-test of this sort will be computed on the bins used by the FFT procedure to produce the original multitaper estimate of the spectrum. It is highly advantageous, indeed necessary, to zero-pad the original data set in order to increase the resolution of the FFT before performing a F-test, as the possible resolution of this test is often greater than Rayleigh resolution, or, $\frac{1}{N}$. Thus, it is actually possible to distinguish, at a suitable signal-to-noise ratio, line components in data that are actually closer than $\frac{1}{N}$ in frequency.

Chapter 4

Pre-Analysis

This section of our thesis is concerned primarily with the work that had to be done to get the data in a form such that it could be analyzed. While this may seem trivial to those who have never had to do it, the work in this chapter took up over 80% of the total time spent on this thesis, and was at times frustrating, exhausting, exhilarating, and annoying.

4.1 Gap Filling

Our original data comes with some holes, mainly obtained through communication error from the Voyager 2 spacecraft. These data points have been flagged in the data set, and must be filled in some way before meaningful analysis can be done.

One extremely simple way to remove the missing points is to simply use a moving average filter which ignores all missing points and computes an average over some K points around the missing point. This average is then used to *plug* the hole.

Ignoring the obvious statistical problems with this method, it does have one thing

going for it: simplicity. It is extremely easy to implement, and fast to run, and has no computational problems whatsoever. However, while simple, there are concerns that gap-filling performed in this way would not be true, as a representation of the data set.

Accordingly, we performed two test runs. The first consisted of using a moving-average filter over 100 points to fill missing points. The filter simply found the 100 points nearest to a missing point, and computed an average, then filled the gap and moved on. We were careful to not use any gap-filled data in further gap-filling, carefully flagging each data point as *original*, *filled*, or *missing*. In this way the filled point for each data gap was dependent only upon the actual data present in the set.

To parallel this test run, we used a much more rigorous gap-filling method, involving both Linear Predictors and a Weiner interpolator. First, the data was scanned and all missing data values were gap-filled using a basic linear interpolations scheme. We then estimated the spectrum, and using its Fourier transformation, obtained an auto-covariance sequence (ACVS) of lag-200. Computing the residuals from this ACVS, we examined the data for outliers, and used a basic linear interpolator to remove them. In this step, we used the ACVS estimate again to estimate the residual sequence, and used the relative error calculation as our determination for clipping outliers. Finally, the gap-filled and cleaned residual data set was recombined with the original ACVS to form our final estimate of the data.

It should be noted that most of the figures shown in this section are of the first 30 hours of data, for ease of plotting and detailed viewing. There were no major differences among the different stretches of time, with the exception of the 6 days around closest approach, when power levels rose more than 10 dB.

Table 4.1: Format of Original .TAB Files

Example	Chars	Content
1979-06-20	10	Date
T00:00:00.334Z	14	Time
20061:22:001	12	Denoted as Julian Days (not actually)
1	4	Instrument Number
0.058	10	Axis-1 (X_{HG}) Magnetometer
-0.0391	10	Axis-2 (Y_{HG}) Magnetometer
0.383	10	Axis-3 (Z_{HG}) Magnetometer
0.550	10	Magnetic Field Magnitude

4.1.1 Moving-Average Filter

The implementation of the moving-average filter is extremely easy. Our original data comes as a ASCII text tab-delimited file, as described in part in Table 4.1.

A simple once-over computer parse of this picks out the different magnetometers, and splits them into separate data sets. We must carefully determine which data points are signal and noise. Thankfully, the authors of the original data file were thoughtful enough to flag all known missing points in a clear systematic way. Any missing point known to the original dataset compilers were flagged and the value replaced by 9999.999.

The spacecraft uses a 3-axis fluxgate magnetometer, and there are two data sets available, consisting of the same raw readings displayed by coordinate system. Two coordinate systems are used: Inertial Heliographic (IHG) and Heliographic (HG). The IHG coordinate system is used to define the spacecraft's position, with the origin defined as the Sun. There are three orthogonal axes: X_{IHG} , Y_{IHG} , Z_{IHG} . The Z_{IHG} axis points northward along the Sun's spin axis, with the $X_{IHG} - Y_{IHG}$ plane lying in the solar equatorial plane. The intersection of the solar equatorial plane with the

ecliptic defines the longitude of the ascending node, which is taken to be the X_{IHG} axis.

The magnetic field orientation is defined with respect to the spacecraft. If we draw a line from the origin of the IHG coordinate system to the spacecraft we define an X - *axis* (Axis-1 in Table 4.1). We define the origin of the HG coordinate system as the spacecraft itself, and point the X_{HG} axis radially away from the Sun. Placing the Y_{HG} axis parallel to the solar equatorial plane, the Z_{HG} axis is chosen to complete the orthogonal trio.

We create a logical array the same length as the original data set, and flag all missing points with `.false..` Then it is a matter of a few lines of code to parse the reorganized data set and replace all missing points with the average of the nearest 100 valid points. An example of a subset of the data with interpolations done this way can be seen in Figure 4.1.

4.1.2 Linear Predictor

Moving past the admittedly oversimplified gap-filling performed by our moving-average method, we began a much more comprehensive evaluation of the data set. In a similar way, we first set up the data with a flag array `ok(1:ndata)` and recorded all known missing points, *i.e.*, those flagged by the original data set creators. We then ran a simple linear interpolator on this data set. The interpolation scheme simply fills all gaps by connecting the good points on either side of the gap using a straight line (polynomial of order 1).

While admittedly not a robust method for filling gaps (it is not in any significant way superior to the moving-average fill method used previously), it is sufficient to set

ourselves up for the real interpolation which can be performed. The difference (on the same stretch of data as shown in 4.1) between the two schemes is shown in Figure 4.2.

4.1.3 Spectrum Smoother

Once we have filled the gaps in our data using the arguably rough method of linear interpolation, we proceed to smooth the interpolated data using a 97 point filter, with weights chosen as

$$\omega_j = \left(\left(1 - \frac{j}{48}\right) \left(1 + \frac{j}{48}\right) \right)^2, \quad j = -48, -47, \dots, 47, 48$$

with the filter plotted in Figure 4.3. We treat the resultant sequence as a linear predictor, and form the residual sequence, where $x(\cdot)$ is the original linearly-interpolated sequence:

$$x_{lp}(\cdot) = x(\cdot) * \omega_j$$

giving

$$x_{res}(\cdot) = x(\cdot) - x_{lp}(\cdot).$$

The typical fit of the linear predictor is quite good, as can be seen in Figure 4.4. The residuals are typically low, on the order of 5 %, except for obvious cases of outliers, which we will deal with next. The results can be seen in Figure 4.5.

4.1.4 Autocovariance Sequences

Now that we have our residual sequence, we compute a basic multitaper spectrum estimate (`NW=5.0, 8 windows`) and using that spectrum, compute the lag-200 autocovariance sequence. The plot of the ACVS is not especially illuminating, so it is excluded here. Using the ACVS, we re-interpolate the residual series, assuming that all previously flagged data points are again incorrect, and reinterpolate the points, only as a function of the **residual** data series.

We begin by taking the $n = 49$ points surrounding any given missing point (± 24 from missing) and flag all valid (non-missing) data points. Then generate an interpolator using the ACVS and the tagged points, and use the interpolator on the data set to generate a new point. The n is entirely arbitrary, and should be large enough to ensure that there are no gaps in the data set large enough that there would not be sufficient points within range to generate the interpolator from.

After computing the interpolation, we generate a measure of the relative interpolation error. This gives us a way to easily find the **obvious** outliers. We then clip the obvious outliers, and complete our cleaning of the residual sequence. It should be noted that we have just described the actual implementation of the Weiner interpolation technique described in Section 3.12.

4.1.5 Further Work

It is entirely possible to continue the process described above, with some variation, effectively forever. Obsession over cleaning every last outlier from the data is counterproductive, however, as we cannot be sure what points are outliers, and what points are actual data. Having progressed to this stage, we leave our data set in its partially

cleaned state, and progress to the final state of our cleanup: downsampling.

4.2 Downsampling

Our original data set contains slightly over 2.4 million data points, recorded every 1.92 seconds for over 53 days. While we are grateful for the length and quality of the data set, that many points is unwieldy to work with, and recorded on too fine a mesh. With this in mind, we downsample and low-pass filter the data, removing extraneous power at high frequencies, and moving our data set to a sample Δt of approximately 1 minute (actually 57.6 seconds).

To do this we use a low-pass filter of 301 points with a 30:1 decimation factor. The filter is symmetric and acausal, and is designed as described in [30]. Figures 4.6 and 4.7 show the filter and its spectral window.

Examine Figure 4.8 for a comparison of the two methods used for interpolation. Note that the majority of the differences in the two curves are due to having applied the residual outlier clipping to the second set.

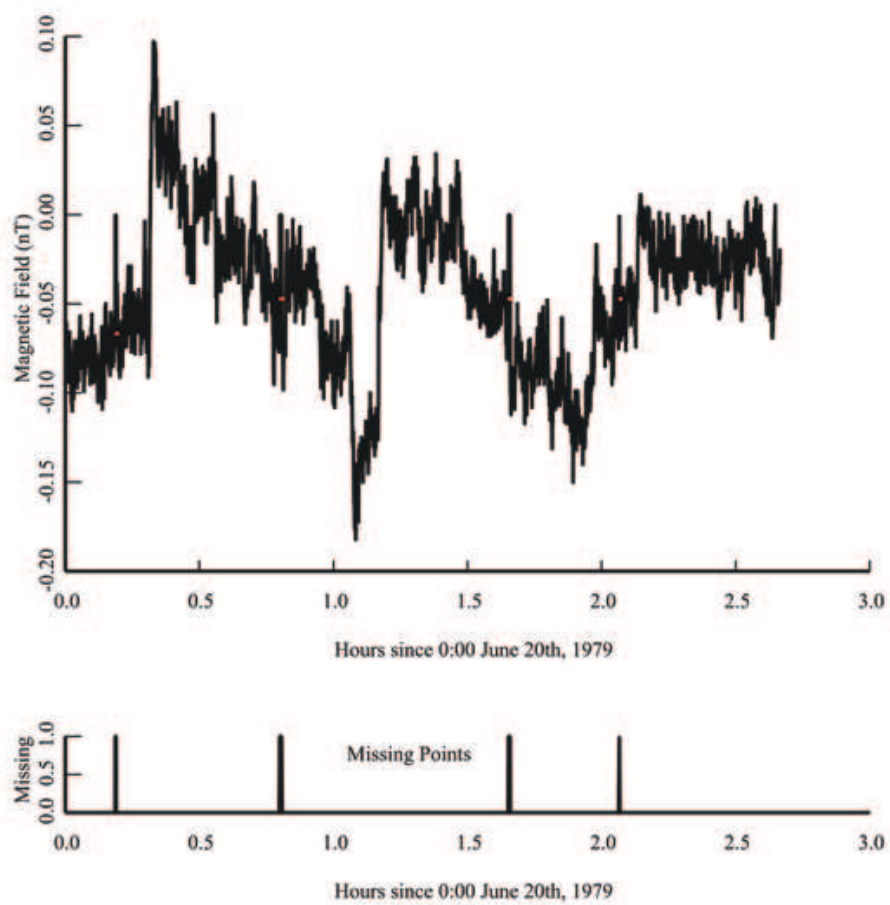


Figure 4.1: Moving-Average Method for Gap-filling (*interpolated data in colour*)
(Note that there were a limited number of replaced points, hence the difficulty in seeing the fill points)

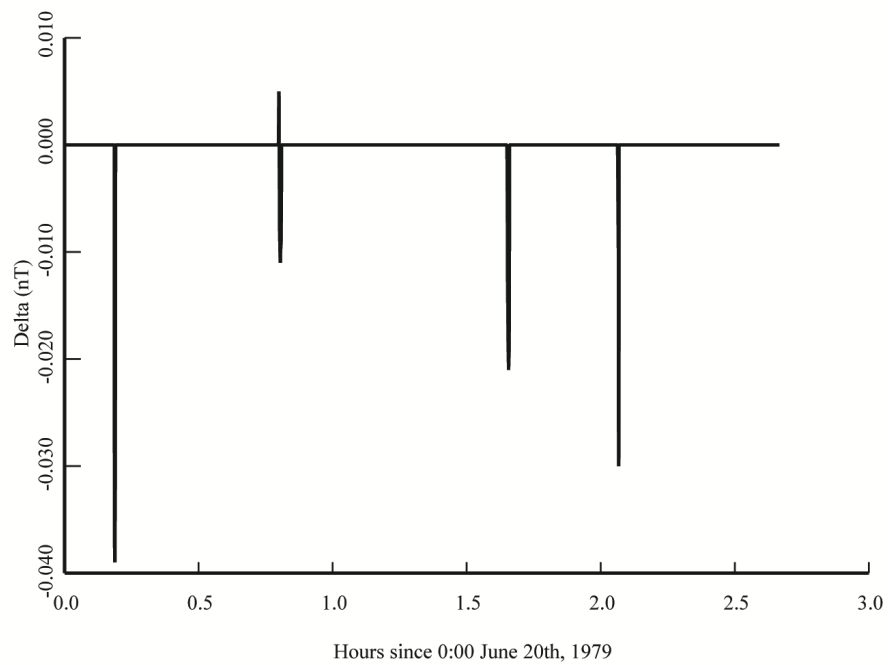


Figure 4.2: Difference between Linear Interpolation and Moving-Average Methods
Note the only differences occur at the gap-filled sites, and are on the order of 20% of the data set magnitude.

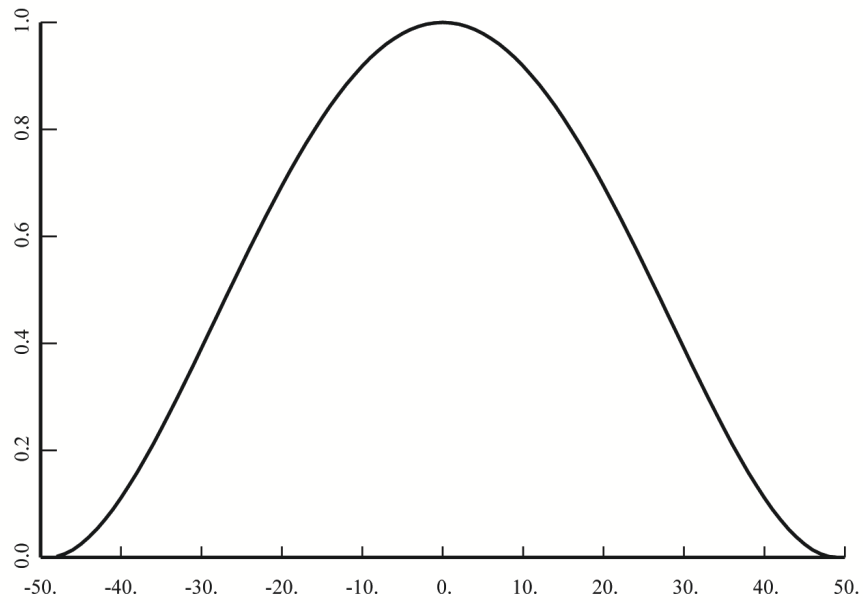


Figure 4.3: Smoother used on Interpolated Data

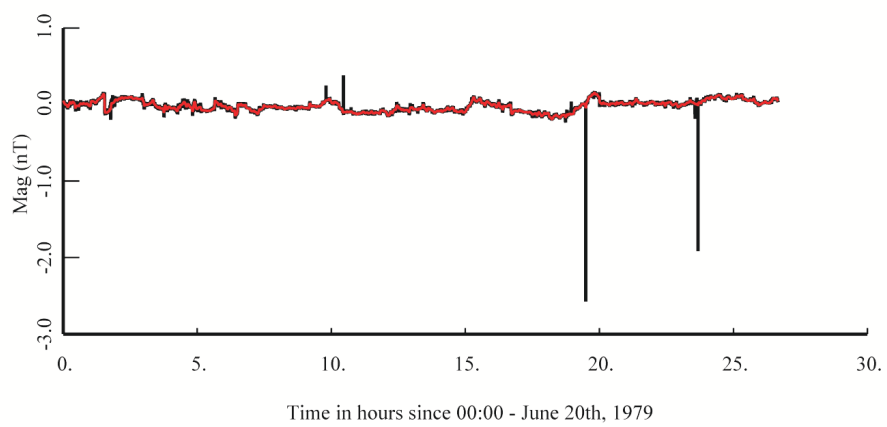


Figure 4.4: Data (black) and Linear Predictor (red)

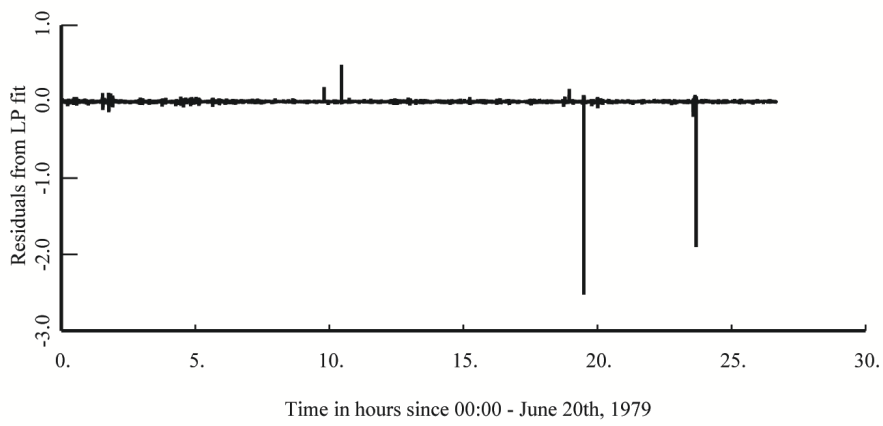


Figure 4.5: Residual Data Series $x_{res}(\cdot)$

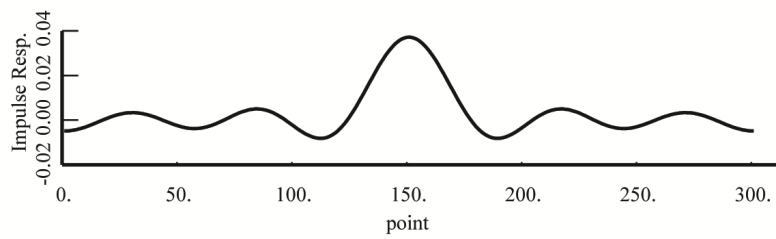


Figure 4.6: 30:1 Lowpass Decimation Filter

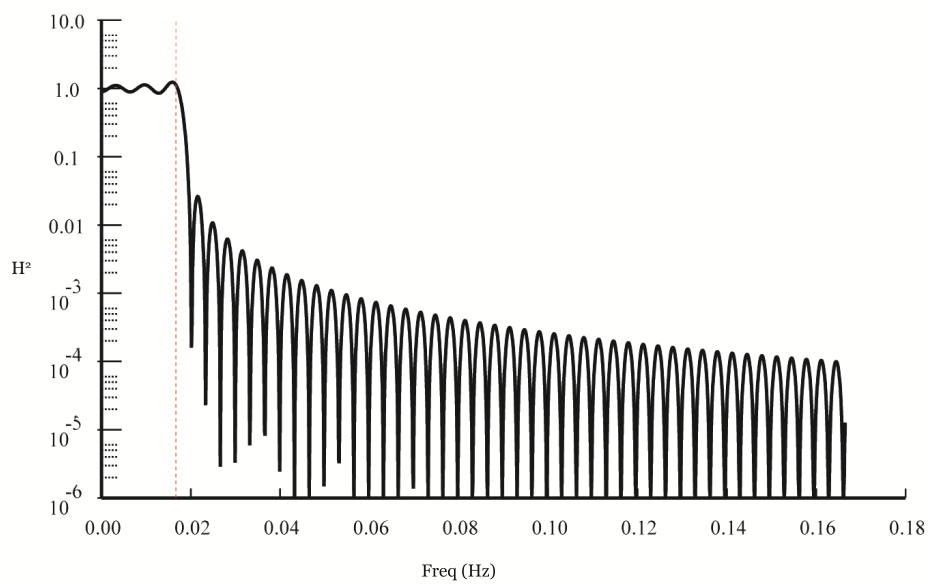


Figure 4.7: Spectral Window

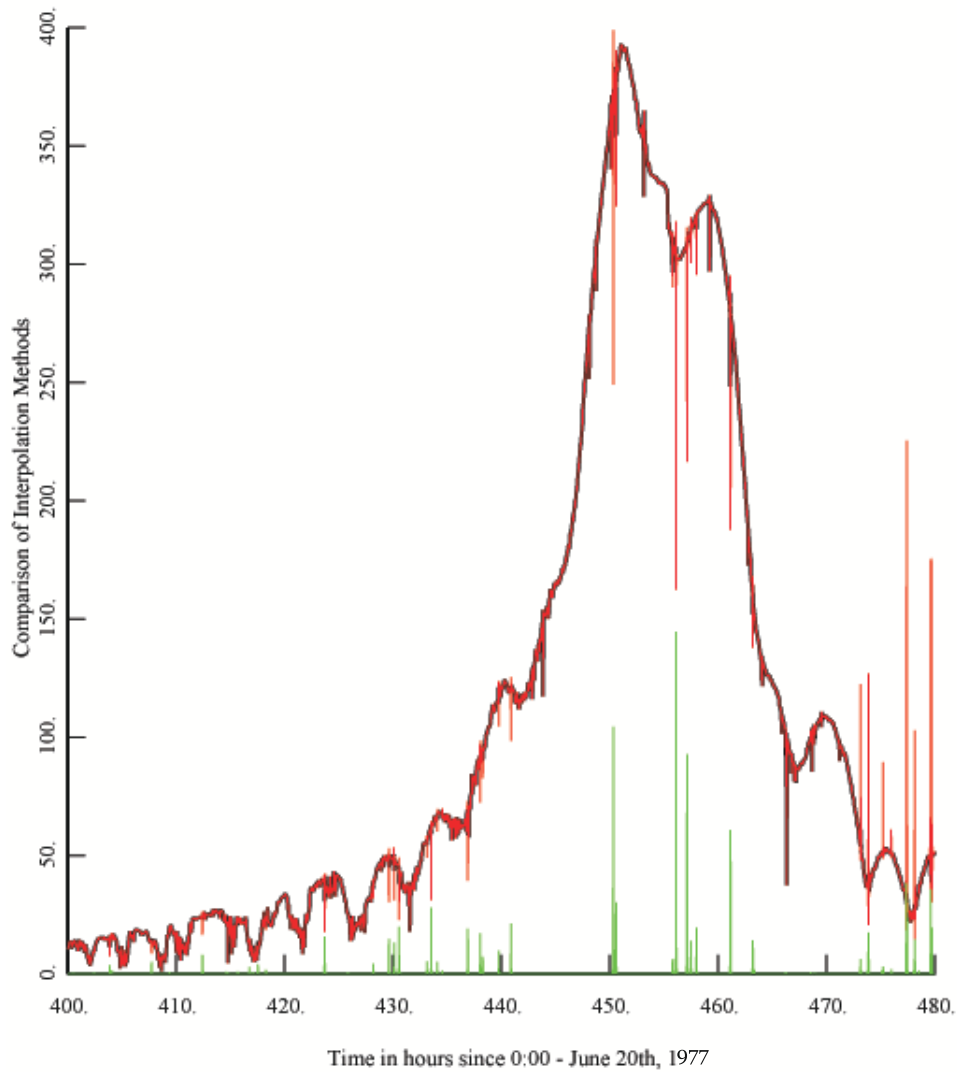


Figure 4.8: Comparison of Interpolation Methods: red is moving-average and black is linear interpolation with outlier clipping. Green is the difference of the two curves.

(Note that the moving-average filter did not have a clipping outlier check run on it, hence the size of some of the differences. Clipping the outliers would result in small differences in the spots where there are large-magnitude results currently.)

4.3 Prewhitening

After completing all the work above, having cleaned some of the outliers, interpolated all missing data points, and having completed the downsampling operation, we have reduced our data set from 2.4 million points to just over 65,000. Each point represents a sample taken approximately every minute, and we retain our three axes of instrumentation along with the net magnetic field in the region. An example of the cleaned data is shown in Figure 4.9.

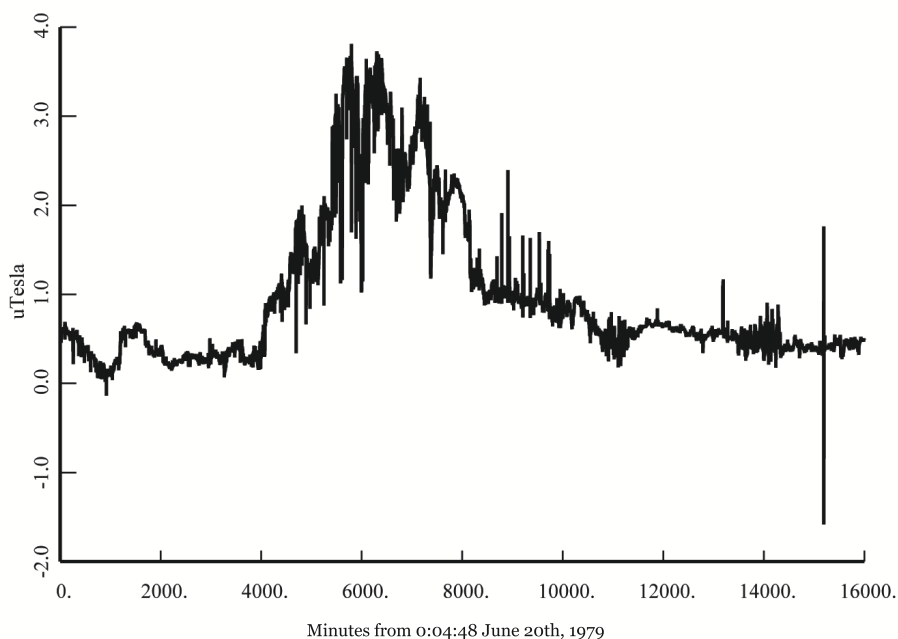


Figure 4.9: Cleaned Data: X-axis

(Note the strange behaviour of the curve, even post-cleaning. It has been suggested that there is some form of magnetic coupling occurring between the fields of Jupiter, its moons, and possibly even the Sun, and that this is causing the strange spikes.)

The initial spectrum estimate for the X-axis magnetometer is shown in Figure 4.10. As we can easily see, the dynamic range of this spectrum is enormous (at least 10^4 if not 10^5). In this situation, we must reduce the range, and thus we turn to a

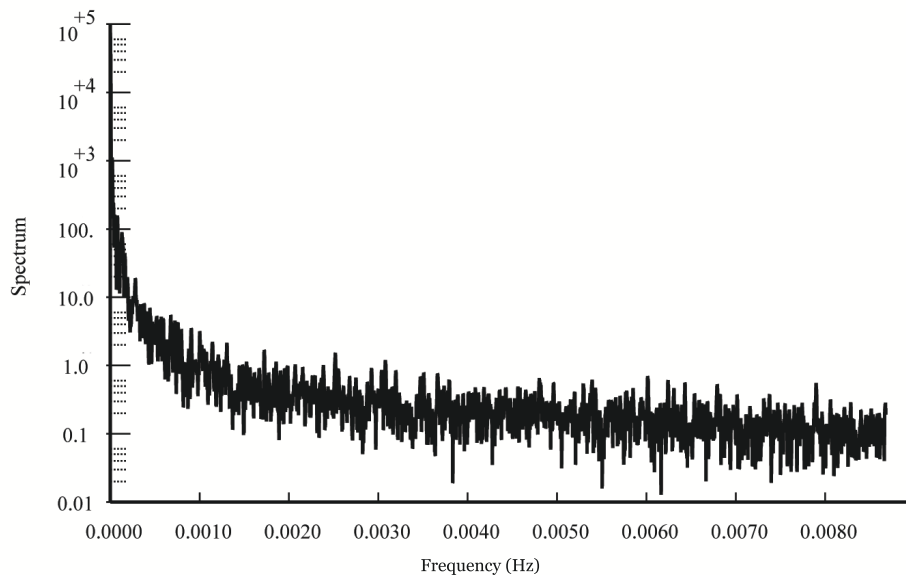


Figure 4.10: Initial Spectral Estimate: X-axis

prewhitening filter.

We compute an initial spectrum estimate using an 8-window multitaper spectrum estimate with $NW=5.0$, and fit several autoregressive (AR) models to it, namely AR-5, AR-15, AR-25, AR-35, and AR-45. Given that our data set length remains so long, despite the decimation and filtering, we chose the AR-45 filter to remove the most easily seen details from the set.

We apply the AR-45 filter to the initial data set, and plot the resultant residual series in Figure 4.11. The resultant spectrum estimate has a **dramatically** reduced dynamic range, as can be seen in Figure 4.12, where the range is at most 20.

4.4 Conclusion

We have prepared all four of our data sets. We have cleaned, pruned, filtered, and prewhitened the data. We have done as much as we can to reduce the bias and dynamic range of the spectrum estimate. The analysis awaits.

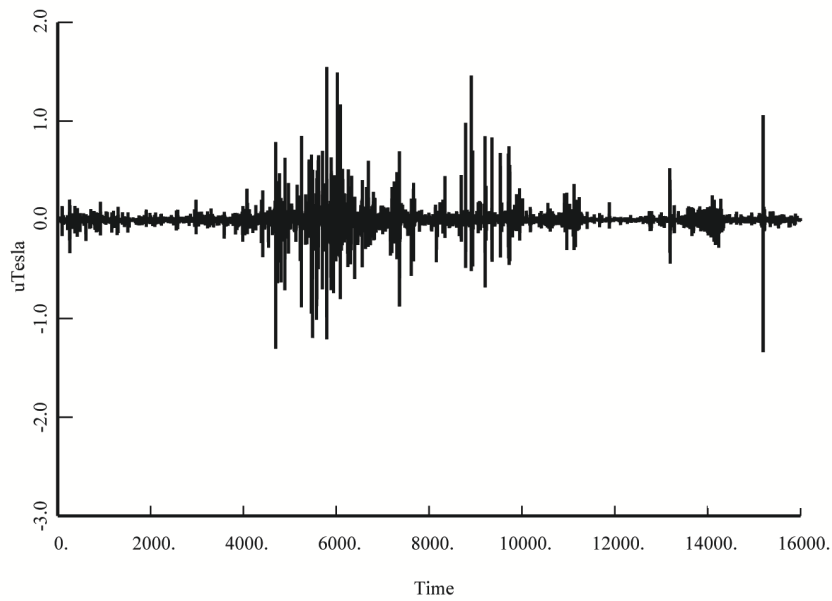


Figure 4.11: Time Series post-AR Filter

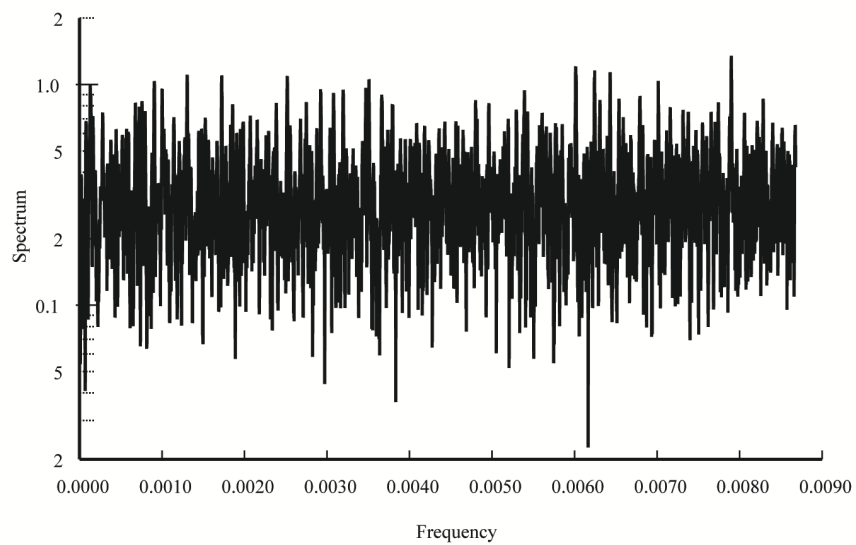


Figure 4.12: Estimated Spectrum Post-Prewhitening

Chapter 5

Analysis

5.1 What to look for?

The data from Jupiter begins on June 20th, 1979, with Voyager 2 still outside the bow shock of Jupiter. The spacecraft would cross the bowshock an estimated 11 times on its way in to closest approach on July 9th, 1979 at 22:29 UTC. The first crossing observed in the data [15] occurred at 16:21 UTC on July 2nd, 1979 and the last at 09:55 UTC on July 5th, 1979.

We are interested in two primary directions for this analysis. The first is the nature of the spectrum **outside** the bow shock, and the second is the nature inside. We hope to show that they are fundamentally different, and tie the pre-bow shock spectrum to the known dynamics of the interplanetary plasma, as detailed in [42] and others. If the nature of the two is fundamentally different, it lends tremendous credence to the idea that the excitations in the plasma surrounding Jupiter are indeed Jovian in origin, and are remnants of modal activity.

Within these bounds on our data set, we are looking for evidence (at high statistical probability) of frequencies of interest, most especially from models given in [19], [6] and [1].

It should be noted at this point that we will make the (arguably) flawed assumption that our data has a spectrum that can be thought of as **central** chi-squared. With the presence of line components, this assumption is not completely reliable, but it does give us an easily tested null hypothesis. See conclusions for more detail as to other routes that are possible for testing.

5.2 The initial F-test

We compute a harmonic F-test on the first 16,000 points in our downsampled sequence, corresponding to the span from June 20th 00:04:48 UTC to June 30th 16:04:48 UTC. This is entirely outside the bow shock of Jupiter, so we do not expect significant results from the planet itself. Instead, we are hoping to show that the character of the spectrum in this time span is that of the spectrum of any stretch of space in the interplanetary medium. This is to say, we hope to show that this spectrum is heavily influenced or even driven by the Sun.

It is quite easy to tell the probabilistic significance of any given result, as the $(1 - \alpha) \times 100\%$ percentage point of the $F_{2,\nu}$ distribution can be found using the equation

$$\frac{\nu(1 - \alpha^{\frac{2}{\nu}})}{2\alpha^{\frac{2}{\nu}}}$$

In our case, the 95% point is equal to 6.07 under the F-distribution. Again, it should be noted that this applied primarily to continuous spectra without the presence

of line components. Against the null hypothesis of a continuous spectrum, if we get a F-test result of 6.0 or more, this is evidence at the 95% confidence level of the **failure** of our hypothesis.

An example of a F-test applied to 16000 points for the net magnetic field is shown in Figure 5.1. It is extremely confusing and crowded, and shows little of interest. We need to go deeper, and focus our viewpoint upon specific frequencies to find the needle in the haystack.

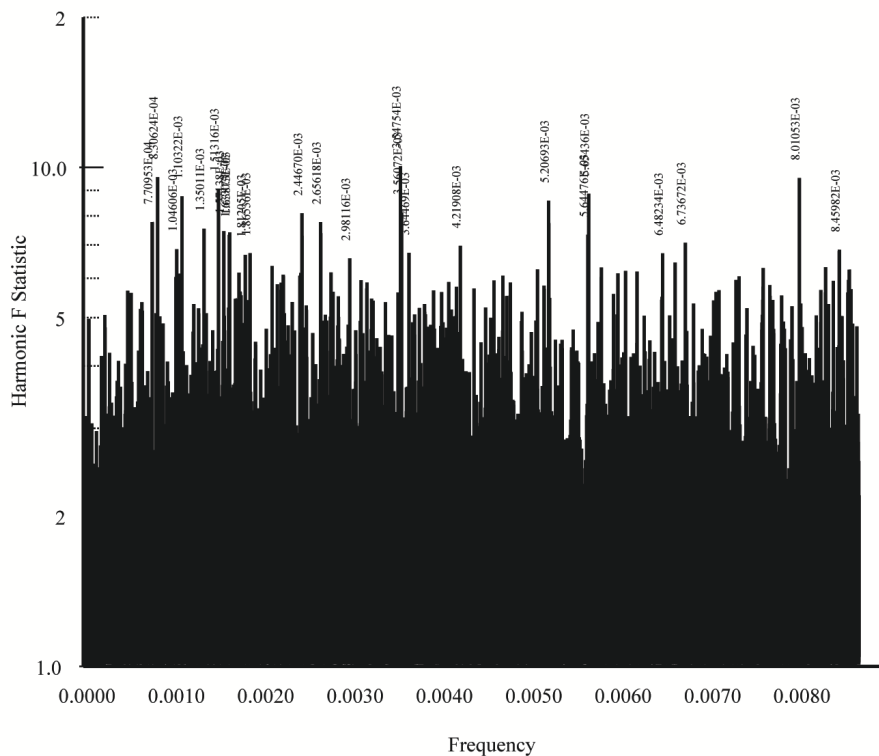


Figure 5.1: F-test with 2, 14 degrees of freedom on spectrum estimate of 16000 points
(Note that in a set of 16000 points, we actually expect 800 false positives at the 95% confidence level, or 6.0. Many of the responses in this image are spurious.)

5.3 Sectioned F-tests

Given the large nature of our data set, and the possible transitory nature of the signals, we must question whether or not a given frequency will be stable enough over the course of weeks or months to actually pass our F-test. We will only accept the hypothesis that the frequency in question is different from background noise if we have a minimum of a 99% significance level. Given that we are dealing with a set of initially 16000 points, we actually expect 1600 false positives at the 90% confidence level, which begs the question: how can we possibly distinguish between noise and signal?

The first method we will use is sectioning our data. Take the 16000 point block of data that is entirely before the bow shock incident. Break the block into 8 distinct sections, each of 2000 points. Compute a multitaper spectrum estimate on the block, using identical characteristics, and then compute a frequency variance test. If a given frequency bin appears at the 95% significance level (say) for **a number of** the 8 tests, it is much more statistically likely to be a true positive, rather than a false.

The math is quite simple. If we assume we have 8 sets, each of 2000 points, and we compute a F-test on each, the probability of a having the same frequency in 5 of the 8 sets (at the 95% significance level) can be approximated as a binominal distribution, *i.e.*, $(0.05)^5(.95)^3$ (8.c.5) $= 1.5 \cdot 10^{-6}$. We would expect to see at least 100 false positive hits at the 95% level for a single set; if we extend this to false positives in 4 of the 8 sets (on the same bin), we reduce our total expected number to less than 1. At 99%, we have a higher probability of being struck by lightning twice than of having a false positive result in 4 of 8 sets (actually 1 in 1.5 million).

This division allows us a simple way to separate the wheat from the chaff, as it

were. The results from the F-test on the 16000-point block were completely inconclusive. There were a large number of hits at high significance levels, but no real way to distinguish between spurious false positives and actual results. Table 5.1 lists the initial results from our analysis of the three magnetometers and indicates frequencies of interest. Any significant result from any of the sets is listed, along with the corresponding results from the other sets.

Table 5.1: F-test Results on the Pre-Bow Shock Data: 90% significance test on 8 sets. Analysis performed on zero-padded 4096-sample set

Bin	Frequency		B_x	B_y	B_z	$ B $
362	1.534	mHz	1	4	0	1
383	1.623	mHz	2	4	1	2
422	1.789	mHz	0	4	2	1
547	2.318	mHz	0	4	2	2
548	2.323	mHz	0	4	1	1
605	2.564	mHz	4	0	2	2
614	2.602	mHz	4	1	1	1
623	2.641	mHz	1	0	4	2
624	2.645	mHz	1	0	4	1
646	2.738	mHz	4	0	1	2
731	3.098	mHz	4	0	0	1
881	3.734	mHz	0	0	4	2
921	3.904	mHz	4	0	0	0
945	4.005	mHz	4	1	2	0
1096	4.645	mHz	1	0	4	3
1098	4.654	mHz	4	1	1	0
1141	4.836	mHz	0	1	4	3
1167	4.946	mHz	2	1	4	1
1395	5.913	mHz	4	2	0	0
1707	7.235	mHz	5	0	1	1
1804	7.646	mHz	1	0	4	3
1992	8.443	mHz	3	4	0	0

(Numbers indicate number of sets (out of 8) that have hits in them.)

We recall that there is some evidence for modal splitting and movement, as per

[43]. Standard deviations in the analysis done by Thomson *et al.* were typically on the order of 0.2 to 0.4 μHz , which in comparison to our bin size is insignificant. We most definitely cannot assume there is frequency shifting on the order of 10 times the average standard deviation.

Comparing the results found here to those in [43], it seems clear that the magnetic field data is not as sensitive to solar influences, at least this close to Jupiter. The analysis done by Thomson *et al.* was done on data from sections of the Ulysses and Voyager 2 orbits away from planetary influences.

In an attempt to refine our analysis, we extend the zero-padding on our 2000-point blocks to 8192 points, and re-analyze the data. Table 5.2 lists all significant results.

Table 5.2: F-test Results on the Pre-Bow Shock Data: 90% significance test on 8 sets. Analysis performed on zero-padded 8192-sample set

Bin(s)	Frequency	B_x	B_y	B_z	$ B $
548-9	1.163 mHz	2	5	1	1
552	1.170 mHz	2	3	5	3
566	1.200 mHz	5	1	1	2
610	1.293 mHz	2	2	6	2
657	1.392 mHz	1	2	5	3
662	1.403 mHz	5	5	1	2
670	1.420 mHz	5	2	2	2
719-25	1.530 mHz	4	6	5	4
731	1.549 mHz	3	5	1	0
736-41	1.562 mHz	3	4	4	2
763-66	1.619 mHz	6	6	4	5
800-02	1.695 mHz	5	5	1	0
810	1.717 mHz	2	5	3	2
819	1.736 mHz	5	1	3	1
843-4	1.787 mHz	2	7	3	4

continued on next page

<i>Continued from previous page</i>						
Bin(s)	Frequency		B_x	B_y	B_z	$ B $
876-7	1.859	mHz	1	0	5	5
919	1.948	mHz	5	2	3	2
934	1.979	mHz	2	2	5	2
993-4	2.104	mHz	3	3	6	2
1009-12	2.143	mHz	5	4	5	3
1040-41	2.204	mHz	0	8	4	4
1051	2.227	mHz	6	1	2	2
1072	2.272	mHz	2	5	3	0
1076	2.280	mHz	5	1	2	2
1136	2.407	mHz	2	2	5	1
1198-99	2.541	mHz	5	2	2	3
1201	2.545	mHz	5	4	4	5
1228-29	2.602	mHz	5	1	1	3
1246-48	2.643	mHz	3	0	7	3
1250-51	2.649	mHz	1	5	3	4
1291-92	2.393	mHz	5	2	5	4
1315-16	2.787	mHz	6	3	2	2
1327	2.787	mHz	1	1	5	3
1332-35	2.812	mHz	6	4	3	3
1362-68	2.893	mHz	5	6	3	3
1395	2.957	mHz	5	3	3	1
1424	3.018	mHz	5	0	1	2
1453	3.079	mHz	5	2	1	2
1458	3.090	mHz	2	3	5	4
1462	3.098	mHz	5	3	0	4
1464-66	3.105	mHz	4	5	1	4
1497	3.173	mHz	3	1	6	2
1523	3.228	mHz	0	2	5	0
1526-30	3.238	mHz	5	2	4	4
1532-34	3.249	mHz	3	2	5	4
1551	3.287	mHz	2	5	3	0
1559-63	3.306	mHz	3	6	5	5
1604-05	3.399	mHz	3	1	5	2
1632	3.459	mHz	5	4	1	2
1643	3.482	mHz	2	0	5	2

continued on next page

<i>Continued from previous page</i>						
Bin(s)	Frequency		B_x	B_y	B_z	$ B $
1678-79	3.556	mHz	5	2	2	4
1697-99	3.599	mHz	1	4	5	4
1737-38	3.679	mHz	1	4	6	1
1754	3.717	mHz	3	1	5	4
1762	3.734	mHz	2	1	5	2
1772-76	3.760	mHz	3	7	4	2
1795	3.804	mHz	3	5	2	2
1823	3.863	mHz	2	5	1	1
1834	3.887	mHz	1	4	5	4
1889-91	4.005	mHz	7	4	4	1
1910	4.048	mHz	5	0	1	1
1916-18	4.062	mHz	5	3	3	7
1924-25	4.077	mHz	2	3	5	4
1935-39	4.105	mHz	6	5	5	0
1989-90	4.215	mHz	6	4	2	0
2031	4.304	mHz	1	2	7	2
3413-14	7.233	mHz	5	1	1	1

There are some significant hits in the increased resolution analysis that may indeed indicate modal structure to the interstellar medium. If we can isolate these modes, we'll have an approximate model for the background noise of the space surrounding Jupiter, which will give us a tool to analyze the data from inside the bow shock.

We begin with a look at the structure around frequency 4.06 mHz, bin numbers 1910-1920. See Figure 5.2 for the four separate data sets, each with an 8-set F-test performed, and all results plotted.

Observe the similarities between B_z and $|B|$, especially with respect to the obvious splitting occurring in the first line (first 2000 points test). The center of the two peaks lines up precisely with the center of the peak located at 4.06 mHz. It should also be noted that the red peak from Set 5 is offset by -0.1 to -0.15 mHz in all cases, while the peak from Set 3 is offset by +0.1 mHz in the case of B_x and B_z .

Can we explain the splitting and the offsets through the different sets? There is

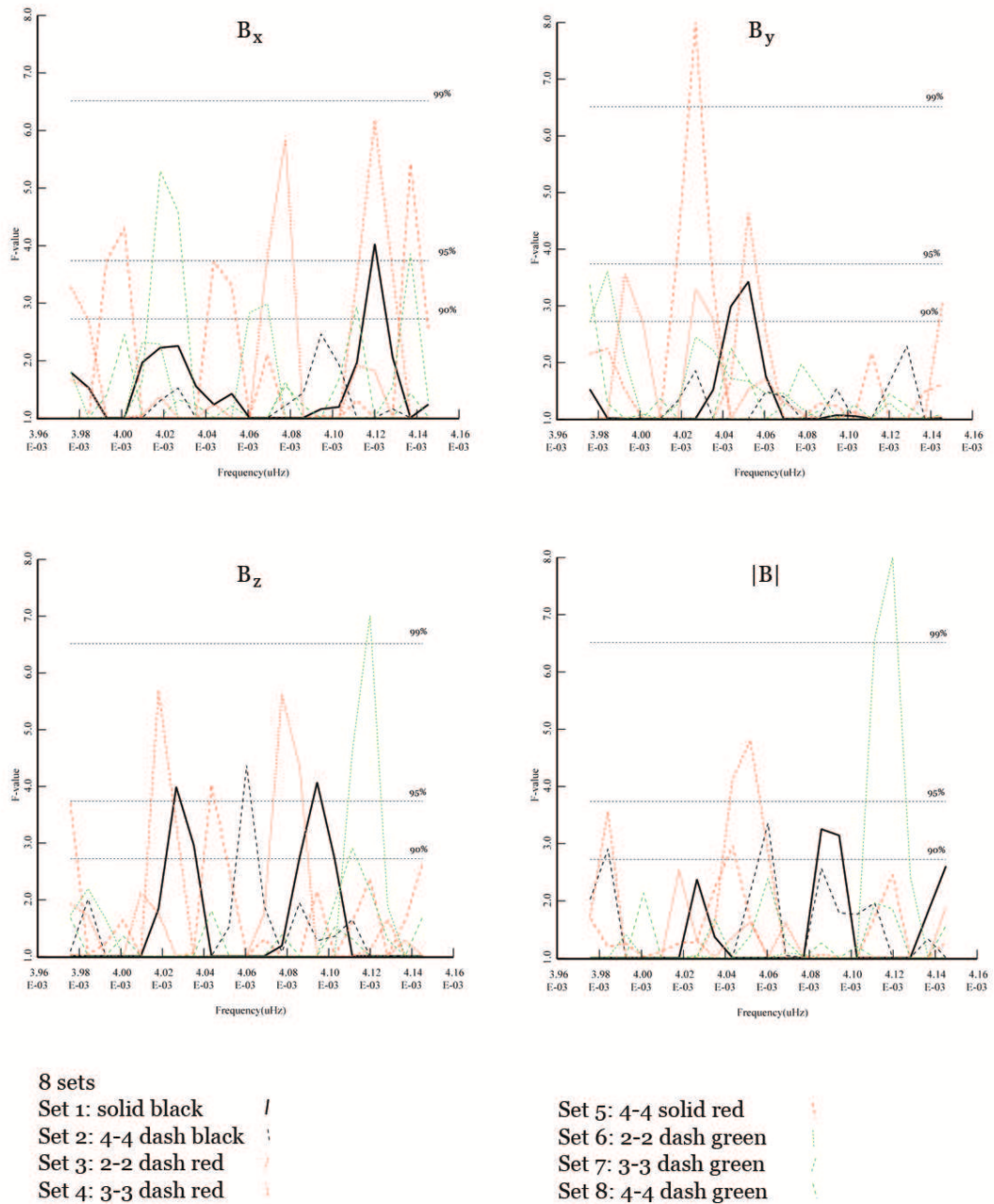


Figure 5.2: F-test Results for Area around 4.06 mHz: Four Data Sets

evidence of some frequency shifting for solar p-modes, especially in the interstellar medium, as well as splitting at the fundamental frequency multiples of the solar core rotation ($n \cdot 1.11 \mu\text{Hz}$). Ness *et al.* note that there is evidence [15] for a periodic fluctuation in the data due to crossings of the near-equatorial current sheets of the magnetosphere, which corresponds to $28 \mu\text{Hz}$. Jovian rotation occurs at a frequency of $27.988 \mu\text{Hz}$, which is what causes the current sheets to move over the spacecraft, causing the fluctuation.

In Figure 5.3, there is definitely evidence for a mode at frequency 1.19 ± 0.05 mHz. There are several splittings (especially in B_y), with some non-split modes at the central frequency.

Doing similar *ad hoc* analysis on some of the other frequencies of interest, we find that there is reasonable evidence for modal structure at the frequencies list in Table 5.3. This table is constructed using qualitative examination of the F-test responses around the frequencies in question. A **strong** result is one in which there exists a strong central peak, and at least one supporting peak; this is to say, in at least one of the eight data sets, there was statistical evidence at the 95% or higher confidence level to accept our alternative hypothesis that this mode exists in the data. A **moderate** response is one in which there are least three supporting peaks at the 90% confidence level (whether central or split around the central frequency). A **weak** response is one in which there is some activity in area, but not of significant statistical value (*i.e.* no peaks above 90%, even if the pattern holds from the other axes).

Of significant interest is the comparison of this rudimentary table with that of [43]. While the table in [43] is incomplete due to space concerns (covering only 2.3 to 3.8 mHz), all frequencies in Figure 5.3 with ‘*’ are coincident between the two

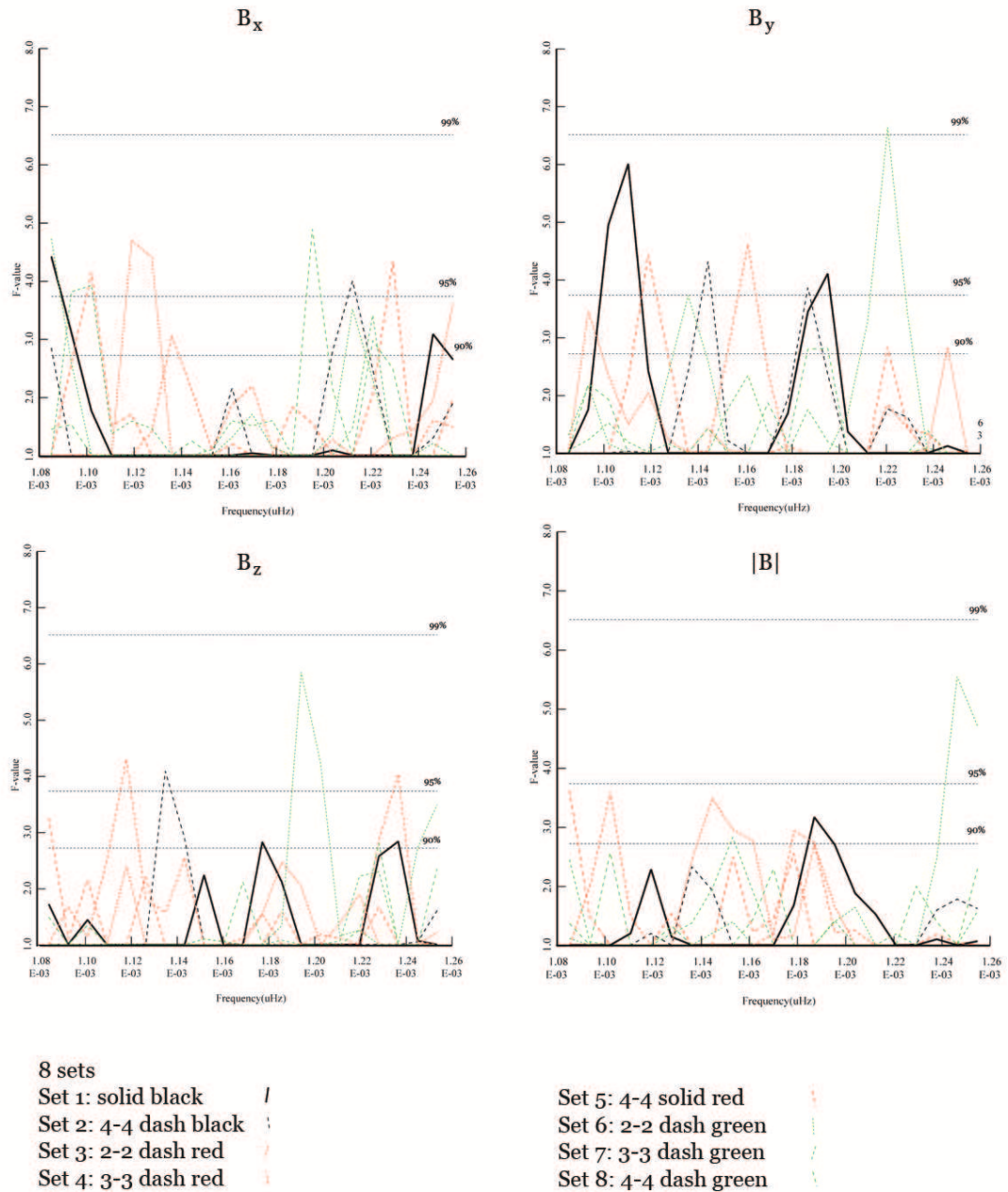


Figure 5.3: F-test Results for Area around 1.19 mHz: Four Data Sets

Table 5.3: F-test Results: Significant Frequencies from Pre-Bow-Shock Data

Frequency		B_x	B_y	B_z	B_{mag}	
1.19	mHz	weak	strong	moderate	moderate	
1.53	mHz	weak	strong	strong	strong	
1.63	mHz	moderate	weak	strong	strong	
1.79	mHz	weak	strong	strong	strong	
2.10	mHz	strong	strong	weak	strong	
2.15	mHz	strong	strong	strong	strong	
2.19	mHz	strong	strong	strong	weak	
2.56	mHz	moderate	strong	strong	strong	*
3.09	mHz	strong	moderate	moderate	strong	*
3.30	mHz	weak	moderate	strong	strong	*
3.77	mHz	weak	weak	strong	strong	*
4.02	mHz	moderate	strong	moderate	strong	

(As explained in the text, **strong** refers to a qualitative response including at least one response at 99%, with multiple supporting peaks in excess of 90%; **moderate** refers to a similar situation, but with the primary peak at only 95%, and **weak** refers to responses all below 95%, but grouped in or around the bin in question. If a **none** appears, it indicates absolutely no results for that bin.)

analyses. Given that the results found in [43] are from Ulysses in 1992-1994 and from Voyager 2 in 1985, while our analysis is of Voyager 2 data from 1979, it would be ludicrous to assume that coincident results are not meaningful. The most probable cause of the modes is solar forcing, given the location of the measuring spacecraft and possible causal links.

In the next section, we will examine data from inside the bow shock of Jupiter, and attempt to determine if these frequencies appear again, and if so, with what power. Additionally, we will attempt to determine if there are unique Jovian forcings contained in the data, and attempt to determine their frequencies as accurately as possible.

5.4 Inside the Bow Shock

In this section, we will analyze two separate blocks of data, each covering approximately 9 days. The first will consist of data from just inside the bow shock of Jupiter, through closest approach, and an additional three days past the intercept. The second set will consist of data entirely past Jupiter, and inside the tail of Jupiter (stretching for approximately 0.5 AU). Table 5.4 lists some important dates, and the corresponding point in our current (downsampled) data set, as a reference.

Table 5.4: Voyager 2 Dates of Interest

Event	Year	Month	Day	Data Set Index
Data set begins	1979	June	20	1
Entrance Bow shock	1979	July	2	17500
Entrance shock exit	1979	July	5	22715
Ganymede flyby	1979	July	9	28141
Closest Approach	1979	July	9	28400
Exit bow shock	1979	July	25	49300
End of data set	1979	August	7	65536

As we begin the analysis of the data surrounding closest approach, it is interesting to note the nature of the data, especially as to how it differs between the 3 axes. Observe Figure 5.4, which shows the data sets over the period immediately surrounding closest approach. Note the periodicity of B_x as it travels across the magnetic sheet repeatedly.

The only results shown in Table 5.5 are those with hits in at least 3 of the 4 data sets, and with at least one hit being 3-in-6 internal sets. The expected number of false detects at the 90% confidence level for a single set of size 2000 is 200. When we extend this to 6 sets, and ask for 3 detects, the expected number becomes 4.

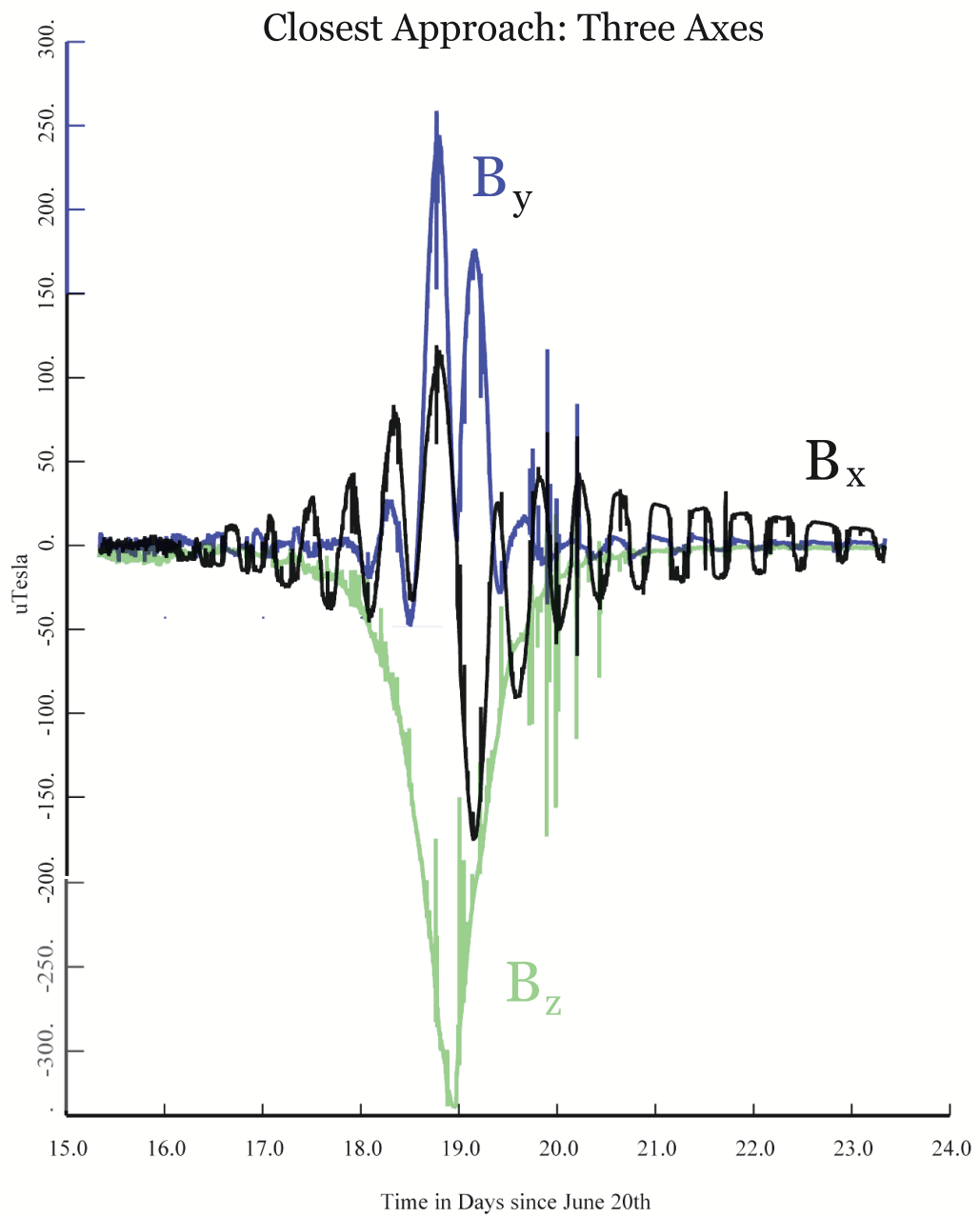


Figure 5.4: Closest Approach

When we additionally force the restriction of detections in three of four **data sets** $(B_x, B_y, B_z, |B|)$, the expected number of false detects at 90% becomes significantly less than 1.

Our first interest is seeing whether or not the frequencies found to be of significance in the pre-bow-shock data persist in this set, inside the bow shock. The **only** frequency from Table 5.3 that *possibly* appears in the post-bow-shock data is that of 4.02 mHz, with a hit at 4.035 mHz. This is 15 μ Hz difference, close enough to warrant a closer look. Figure 5.5 shows the details for the current data sets. It should be compared to Figure 5.2.

Table 5.5: F-test Results on the Closest Approach Data: 90% significance test on 6 sets. Analysis performed on zero-padded 8192-sample set. Only significant results are shown, see the Appendix, Table 7.1 for full results.

Bin(s)	Frequency	B_x	B_y	B_z	$ B $
12-14	27 μ Hz	3	3	0	2
39	82.652 μ Hz	2	1	1	4
40-1	84.771 μ Hz	3	1	1	3
65-8	140 μ Hz	4	3	1	2
124	262.790 μ Hz	0	2	1	3
266-8	565 μ Hz	1	4	1	3
314	665.453 μ Hz	1	3	0	2
456	966.390 μ Hz	1	2	3	0
547	1.159 mHz	2	2	3	1
645	1.367 mHz	2	1	0	3
661-3	1.401 mHz	1	1	2	3
688-9	1.458 mHz	1	0	3	3
869	1.842 mHz	2	0	1	3
927-8	1.965 mHz	1	1	3	2
939	1.990 mHz	1	3	1	1
1025	2.172 mHz	1	0	3	2

continued on next page

<i>Continued from previous page</i>						
Bin(s)	Frequency	B_x	B_y	B_z	$ B $	
1055	2.236	mHz	3	1	3	1
1088	2.306	mHz	3	2	0	0
1100-02	2.331	mHz	1	1	3	3
1170-1	2.480	mHz	1	2	3	2
1199	2.541	mHz	0	2	3	2
1262-3	2.675	mHz	0	3	3	3
1286	2.725	mHz	1	0	3	2
1341-4	2.842	mHz	2	0	4	2
1432-3	3.035	mHz	3	0	3	0
1440-2	3.052	mHz	0	3	1	2
1655	3.507	mHz	3	1	1	2
1835	3.889	mHz	3	2	0	1
1904-6	4.035	mHz	0	1	3	2
2001	4.241	mHz	3	2	2	1

The features in these two figures are quite similar. Examining the B_x plot first, note that in Figure 5.2 the two most significant peaks are located at 4.02 mHz and 4.075 mHz, with the peak (in red) at 4.05 supported by a split pair of peaks at 4.01 and 4.07 mHz (in green). The argument could be made for a moderate result at any of the three frequencies: 4.02, 4.05, and 4.07 mHz. In Figure 5.5 there is a similarly strong result at frequency 4.02 mHz, supported by one main peak significant at 99%, with 3 separate splitting pairs (at $\pm 15\mu\text{Hz}$). There is no comparative result for the 4.03 mHz peak in Figure 5.2, but it is interesting to note that the two 99% peaks in question (4.02 and 4.03 mHz) are split exactly on yet another peak significant at 95%. It is entirely possible that what we are seeing here is frequency shifting on the order of $5\ \mu\text{Hz}$, around a central frequency of 4.025 mHz. It should be noted that solar modes shift in frequency with activity, but a more likely explanation for this shift is a change in velocity due to local plasma conditions.

Comparing B_y , in Figure 5.2 there is a significant result at 4.025 mHz, with a

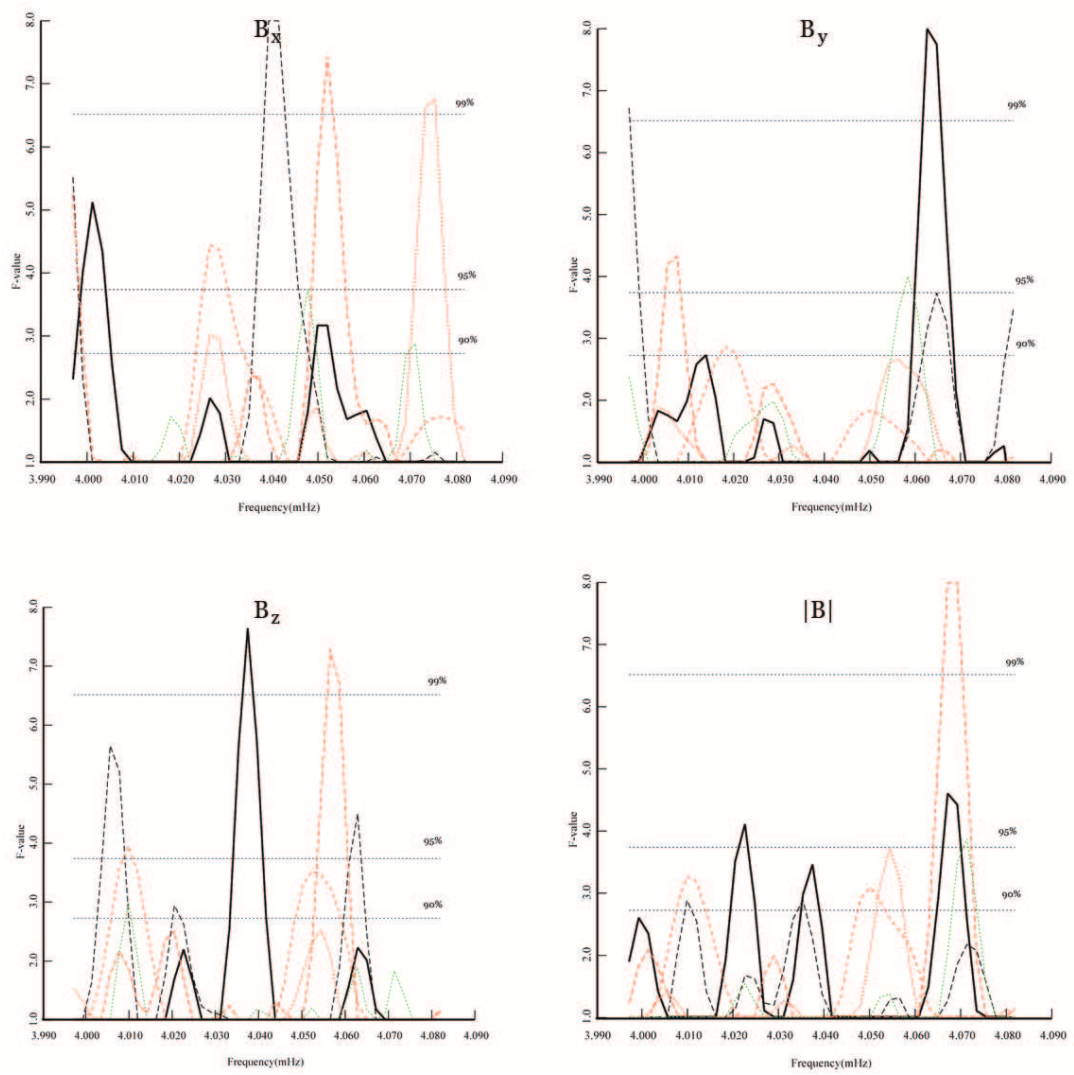


Figure 5.5: F-test Results for Frequencies around 4.06 mHz inside Bow Shock: four data sets

reasonable response at 4.05mHz as well. The significant peak in Figure 5.5 is located at 4.062 mHz. Interestingly, the precise halfway point between the two peaks (in red) in Figure 5.2 is 4.02 mHz.

In B_z , Figure 5.5 has 99% responses (with little secondary peak support) at 4.035 and 4.055 mHz, while Figure 5.2 shows three 95% results at 4.018, 4.024, and 4.060 mHz.

We can thus make an argument for similarities between these two plots. One is inside the bow shock, and the other outside, so theory suggests there could be **some** coupling of modes through the bow shock, especially in the case of exceptionally large Q (Q standing for quality-factor, a term in physics in engineering that ompares the frequency at which a system oscillates to the rate at which it dissipates its energy). We will limit ourselves at this time to stating that for a null hypothesis of a continuous spectrum, we have found (at approximately the 95% confidence level) the hypothesis to be false. There is a frequency of interest in our data at 4.02 ± 0.015 mHz. The confidence interval is calculated by consideration of the Rayleigh resolution for this analysis.

Table 5.6: F-test Results: Significant Frequencies from Closest Approach

Frequency		B_x	B_y	B_z	B_{mag}
27	μHz	strong	strong	none	strong
82	μHz	strong	strong	none ^a	strong
85	μHz	strong ^b	strong	strong	
140	μHz	strong	strong	strong	strong
263	μHz	weak	strong	none	strong
565	μHz	none	strong	moderate	strong
665	μHz	weak	weak	strong	strong
966	μHz	moderate	moderate ^c	strong	weak
1.16	mHz	strong	moderate	strong	moderate
1.37	mHz	strong	moderate	strong	moderate
1.40	mHz	weak	moderate	moderate	strong
1.46	mHz	weak ^d	weak	strong	moderate
1.84	mHz	strong	none ^e	moderate	weak
1.97	mHz	strong	weak	strong	moderate
1.99	mHz	weak	strong	moderate	weak
2.17	mHz	strong	moderate	moderate	moderate
2.24	mHz	moderate	strong	moderate	weak
2.31	mHz	strong	strong	weak	none
2.33	mHz	moderate	moderate	strong	strong
2.48	mHz	moderate	strong	strong	moderate
2.54	mHz	weak	strong	strong	strong
2.68	mHz	none	moderate	moderate	moderate
2.73	mHz	weak	weak	moderate	weak
2.84	mHz	moderate	weak ^f	strong	strong
3.04	mHz	moderate	none	strong	weak
3.05	mHz	weak	strong	moderate	moderate
3.51	mHz	weak	moderate	weak	strong
3.89	mHz	strong	strong	moderate	moderate
4.04	mHz	moderate	strong	strong	strong
4.24	mHz	strong	strong	moderate	weak

^aVery strong result at 56 μHz (twice rotational)^bOverlap between the 82 and 85 μHz peaks^cStrong result at 975 μHz ^dStrong result at 1.475 mHz^eStrong result at 1.83 mHz^fStrong result at 2.83 mHz

We now perform the same qualitative analysis performed for the significant results in the pre-bow shock data. See Table 5.6 for full details.

5.4.1 Post-Jupiter Approach

Continuing to the second set of 12000 points inside the bow shock, we repeat the analysis. Again we take 2000 points at a time, and perform a multitaper spectrum estimate using $NW=5.0$ and 8 windows. After prewhitening the 12000 point set, we found that the dynamic range of the spectrum remained high, so we applied a second AR-45 filter to the already prewhitened data, except on 2000-point blocks, each taken separately. This reduced the range to a much more reasonable result, and we then computed the F-test on this data. See Figures 5.6 and 5.7 for an example of this operation.

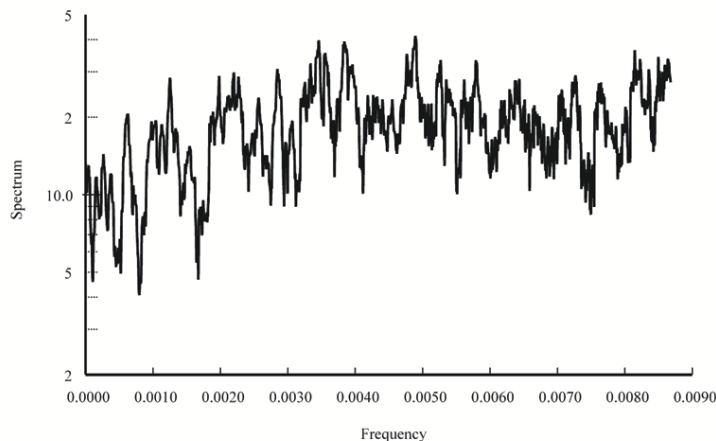


Figure 5.6: Pre-Whitened Data: 2000-point block, 8192-point FFT

Table 5.7 shows the results for the same frequencies chosen for the closest approach. The results from the second set were more *subdued* than the results from closest approach, due mainly to the need for a second prewhitening filter and certain

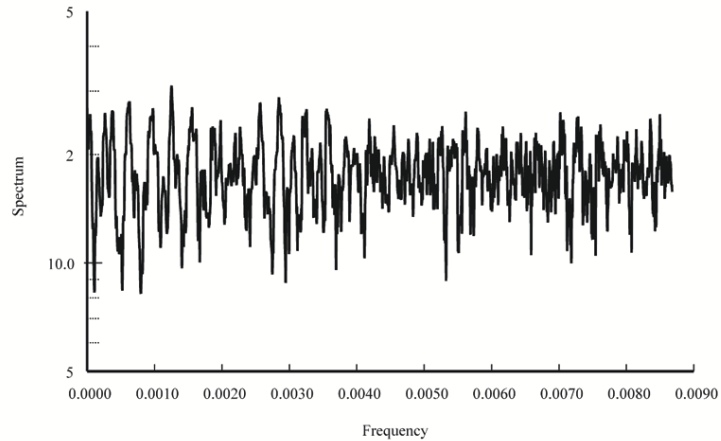


Figure 5.7: Pre-Whitened Data post second Pre-Whitening Filter

inconsistencies in the data. In each block of 2000 there were at least 3 *bursts* of noise, which could be signal, but more likely are interference from Jupiter and its moons, as the spacecraft travelled away from the planet and deeper into the solar system.

At this point in the analysis, we have shown that there is *reasonable* statistical evidence for non-turbulent forcings in the magnetic field data from Voyager 2 around Jupiter. In addition, we have shown that frequencies that are strong and clearly evident in the data from before the bow shock event are, on the whole, **not** replicated inside the bow shock. This lends credence to the theory [22] that the bow shock acts as a dampener. In theory, the field inside the bow shock should be primarily composed of interactions of forcings from Jupiter's modal structure. It is this theory we examine next.

Table 5.7: F-test Results: Significant Frequencies from Post-Approach

Frequency		B_x	B_y	B_z	B_{mag}
27	μHz	strong	strong	strong	strong
82	μHz	weak	weak	moderate	weak
85	μHz	none	none	moderate	weak
140	μHz	none	strong	moderate	weak
263	μHz	moderate	weak	moderate	weak
565	μHz	weak	moderate	weak	weak
665	μHz	weak	strong	moderate	weak
966	μHz	moderate	moderate	moderate	weak
1.16	mHz	moderate	moderate	weak	weak
1.37	mHz	strong	strong	moderate	weak
1.40	mHz	none	strong	strong	weak
1.46	mHz	strong	strong	weak	weak
1.84	mHz	moderate	weak	moderate	none
1.97	mHz	moderate	weak	moderate	weak
1.99	mHz	weak	weak	weak	none
2.17	mHz	moderate	none	weak	weak
2.24	mHz	none	weak	strong	moderate
2.31	mHz	moderate	moderate	strong	moderate
2.33	mHz	weak	moderate	moderate	weak
2.48	mHz	weak	strong	strong	weak
2.54	mHz	moderate	weak	weak	moderate
2.68	mHz	strong	strong	weak	weak
2.73	mHz	strong	moderate	weak	moderate
2.84	mHz	strong	none	weak	weak
3.04	mHz	strong	weak	weak	moderate
3.05	mHz	weak	weak	weak	weak
3.51	mHz	weak	strong	none	weak
3.89	mHz	moderate	strong	strong	moderate
4.04	mHz	none	strong	strong	none
4.24	mHz	moderate	strong	strong	weak

5.5 Comparing Models to Data

We begin by comparing the results and model used by Mosser *et al.* [27] in their 1991 paper. They found a number of $l = 1, m = \pm 1$ doublets in the analysis of their data, which was obtained from a series of night observations using an Earth-based optical instrument. The results are reproduced below in Table 5.8, with our results added in the last column. Our results are taken from visual examination of F-test results for the B_x data, during the 12000 points around closest approach.

Table 5.8: Results from Mosser *et al.* [27]: $l = 1, m = \pm 1$

Mosser (μHz)	Δf	Mean (μHz)	Model	Our Results (μHz)	Δf
569-625	56	597	557-613	568-627	59
680-732	52	706	673-729	679-734	55
793-853	60	823	792-848	790-849	59
919-979	60	949	917-973	919-979	60
1300-1356	56	1328	1307-1363	1304-1360	56
1436-1490	54	1463	1438-1494	1425-1490	65
1568-1624	56	1596	1568-1624	1567-1627	60
1702-1756	54	1729	1694-1750	1701-1757	56
1816-1868	52	1842	1814-1870	1814-1872	58
1928-1980	52	1954	1929-1985	1923-1979	56
2178-2236	58	2207	2166-2222	2175-2231	56

(Note the extremely close correspondance between our results, Mosser's results, and the model predicted frequencies. Every single mode has a hit, and a close one at that.)

We note the extremely close correspondance between the two sets. Admittedly there is no strong statistical evidence for us to define how rigorously these peaks exist in the data, but as a random check of the validity of our results, it is intriguing. Every single doublet mentioned by Mosser *et al.* [27] exists in our data set (for B_x), and is within 5 μHz for the pairing. This leads us to conclude that there is Jovian forcing occuring in this data set.

We continue with a comparison of the results from Mosser *et al.* [29] in their 1992 paper, where the data was recorded using the same instrument. In Table 5.9 we compare their results with B_y data values from our data, using the 12000 points around closest approach. Note the Δf values, and reference Section 6 for an explanation.

Table 5.9: Results from Mosser *et al.* [29]: $l = 2, m = \pm 1$

Mosser (μHz)	Δf	Mean (μHz)	Model	Our Results (μHz)	Δf
751-813	62	782	757-813	755-816	61
887-939	52	913	891-947	882-945	63
1020-1080	60	1050	1022-1078	1019-1079	60
1280-1336	56	1308	1276-1332	1276-1334	58
1409-1459	50	1434	1401-1457	1397-1455	58
1530-1586	56	1558	1524-1580	1520-1577	57
1650-1700	50	1675	1647-1703	1647-1710	63

Again, for every frequency in the list, there is a significant F value for at least one, and often many, of the 6 sets used to create the plots. The correlation is evident: Jupiter is driving the magnetic field in its vicinity at normal mode frequencies. This is not particularly a surprise to us, but it does confirm that the data we have will actually provide a viable medium for search of Jovian p-modes, and possibly g-modes.

5.5.1 Gudkova Model Comparison

We now reference the paper by Gudkova and Zharkov [19], which developed several models for the free oscillations of Jupiter. Their table is quite extensive, and gives periods for modes that should result from phase-barrier transitions inside the planet, for $l = 1, \dots, 10$.

We concern ourselves primarily with the model MJ3 from their paper, and reproduce (in part) the table they give. We add our results to the table as a separate

Table 5.10: Results from Gudkova and Zharkov [19]: $l = 1, \dots, 10$

		$l = 1$	$l = 2$	$l = 3$	$l = 4$	$l = 5$
Per. (min)	1	2406	1619	1223	1000	855.9
Freq. (μHz)		6.27	10.3	13.6	16.7	19.5
Result		N/A	N/A	N/A	N/A	N/A
		$l = 6$	$l = 7$	$l = 8$	$l = 9$	$l = 10$
Per. (min)	1	754.5	653.9	579.7	521.5	474.6
Freq. (μHz)		22.1	25.5	28.8	32.0	35.1
Result		N/A	N/A	30	30	37
		$l = 1$	$l = 2$	$l = 3$	$l = 4$	$l = 5$
Per. (min)	2	687.3	410.6	301.5	242.9	206.4
Freq. (μHz)		24.2	40.6	55.3	68.6	80.7
Result		27	39	55	N/A	81
	2	$l = 6$	$l = 7$	$l = 8$	$l = 9$	$l = 10$
Per. (min)		181.6	163.7	150.1	139.4	130.8
Freq. (μHz)		91.8	101.8	111.0	119.6	127.4
Result		88	N/A	111	119	127
		$l = 1$	$l = 2$	$l = 3$	$l = 4$	$l = 5$
Per. (min)	3	150.9	81.60	64.24	55.04	48.92
Freq. (μHz)		110.4	204.2	259.4	302.8	340.7
Result		111	201	259	303	340
		$l = 6$	$l = 7$	$l = 8$	$l = 9$	$l = 10$
Per. (min)	3	44.45	41.00	38.23	35.96	34.05
Freq. (μHz)		375.0	406.5	436.0	463.5	489.5
Result		377	399	436	459	490
		$l = 1$	$l = 2$	$l = 3$	$l = 4$	$l = 5$
Per. (min)	4	179.4	110.8	85.18	71.88	63.61
Freq. (μHz)		92.9	150.4	195.7	231.9	262.0
Result		86	N/A	197	233	260
		$l = 6$	$l = 7$	$l = 8$	$l = 9$	$l = 10$
Per. (min)	4	57.82	53.44	49.95	47.09	44.67
Freq. (μHz)		288.3	311.9	333.7	354.0	373.1
Result		288	309	334	N/A	376

(N/A refers to absolutely no comparative frequency in our analysis. Result refers to to our discoveries in this analysis.)

row. Results for this table are taken from $|B|$. N/A indicates a result for which there was no significant (95%) peak within $5 \mu\text{Hz}$. In a few instances, a number has been recorded if the peak is of special note (99%+), even if outside our self-imposed boundary of $\pm 5 \mu\text{Hz}$.

The model MJ3 was chosen as it was the primary focus of the paper in question, and was the first model to truly integrate the concept of a metallic hydrogen core, with assumptions of phase changes around the core as the pressure caused the hydrogen form to mutate.

The results are similar to what we have found previously. There are a number of superb coincidences, with frequencies predicted and observed accurate to $\pm 1 \mu\text{Hz}$. There are a number of elements with the frequency in question falling directly between two significant peaks. Specifically, the frequencies in Table 5.11 are those for which there is significant statistical evidence. Under the assumption that the probability of a false detect on any given set is independent of any other set, we compute a rough gauge for the probability of a false detect of frequencies in this table, based on the F distribution values obtained for the 6 sets.

Table 5.11: Significant Results from Gudkova and Zharkov [19]: $l = 1, \dots, 10$

Frequency	$l =$	Transition	P(false)
55.3 μHz	3	2	1 in 200,000
259.4 μHz	3	3	1 in 80,000,000
80.7 μHz	5	2	1 in 4,000,000
333.7 μHz	8	4	1 in 50,000
489.5 μHz	10	3	1 in 2,000,000

Chapter 6

Summary and Conclusions

6.1 Summary

We began with data from Voyager 2, recorded in .TAB files. This data had numerous gaps, outliers, and was generally unformatted. We formatted and cleaned the data, filled the gaps using a linear and Weiner interpolation scheme. The data was then lowpass decimate filtered, resulting in a final data set of approximately 70,000 points, recorded at 57.6 second intervals.

After rudimentary examination of this data set using a multitaper spectrum estimate ($NW=5.0$, $K=8$), we broke the data into 3 sets for analysis. The first set consisted of points from entirely before the bow shock event on and around July 2nd. These 16000 points were broken into 2000-point sets, and spectra estimated for each. These spectra gave us $AR(p)$ pre-whitening filters which we then applied to the data to reduce the dynamic range. The spectra were then analyzed using the harmonic frequency variance test, which against the null hypothesis of a continuous spectrum gave us the F-distribution value for each FFT bin. The sets were then cross-correlated,

looking for coincidences in the bin slots. Any set with more than 4 hits out of 8 bins was recorded, and evaluated qualitatively from plots produced by the same program.

We found that there were a number of statistically relevant frequencies in this block of data, and recorded them all in Table 5.3.

We then examined two blocks of data inside the bow shock, each 12000 points in length. The first set was centered around the closest approach of Voyager 2 to Jupiter, and consisted of extremely noisy data (due to the conditions near the planet). After some processing, and a procedure functionally identical to the one above, we found a list of significant frequencies for this set as well. Interestingly, only one of the thirty frequencies noted was a match between the closest approach set and the pre-bow-shock set. We evaluated this frequency, and found it to be close enough to be worth noting.

We again performed a qualitative test on the frequencies with coincidences of 3 out of 6 or more. This provided us with a table of frequencies against which to compare Jovian models in the future.

The second set of points inside the bow shock was then evaluated, and found to have poor signal-to-noise, with very little discernable structures. The signal power was much lower in this block than in the closest approach block, but the noise was of roughly equivalent size. We feel this may have damaged this section of data beyond use. Despite the poor quality, we did the analysis of this set in full as in the closest approach, and found again a list of frequencies. The number of notable frequencies was greatly reduced, and we direct the reader to Table 5.7 to examine the qualitative results.

Having done the analysis on the three data sets without any preconceptions as

to what we were looking for, we began going back over the sets and examining them for evidence of Jovian modes, as per the models developed by Gudkova, Zharkov, and Mosser and observations by Mosser *et al.* The comparisons with Mosser's optical observations were particularly interesting, with every doublet found in both papers [27], [29] appearing in our data with reasonable statistical significance. In addition, the values of Δf are in-line with previously found values (by Mosser, especially), and give further credence to the work in [6] which found the characteristic frequency to be $\nu_0 = 142 \pm 3 \mu\text{Hz}$. Determining an accurate value of ν_0 will determine the radius of the planetary core, a particularly thorny problem at the heart of most modelling projects for Jupiter, since we cannot know precisely how the helium-hydrogen interactions occur at the extremely high pressures of the core. This is an ongoing research question.

We continued our comparison with a look at the free oscillation values given by Gudkova and Zharkov in [19]. These values represent frequencies for the phase transitions inside Jupiter, based on a 5-phase model MJ3. We found a number of superb coincidences in this data, along with a number of passable frequencies. It seems obvious that the data recorded by Voyager 2 is actually driven by, and representative of, Jupiter's modal structure.

6.2 Future Work

There are a tremendous number of paths that can be taken from where this research leaves off. It would serve our purposes to do a thorough statistical examination of the data, especially with respect to its base spectrum. We made the flawed assumption throughout this analysis that we were dealing with a **central** chi-square distribution, which is patently false. It serves as a pleasant fiction, and allowed us to complete

the analysis, but to rigorously examine this data, we need to evaluate the level of non-centrality of each spectrum, and perform the harmonic analysis using that as a basis.

Additionally, it would be useful to be able to move from the qualitative analysis done on the frequency variances, and move to a more quantitative analysis, using the statistical technique of jackknifing to determine the variance of each individual frequency estimate. This provides an automated way to distinguish between good and bad results, and would increase the power of this research tremendously.

In addition to statistical improvements, there are improvements in use of multiple data sets that may be of use – difference between coordinates may be a result of local plasma movements or densities giving doppler shifts or velocity changes. Thus comparison of data sets between Voyager, Voyager 2, Ulysses, and even ACE (for background spectrum) will expand the scope of the research.

If more accurate analysis were performed, it may lead to concrete results which could confirm or refocus the analysis performed by Mosser *et al.* in [6], concerning the characteristic splitting frequency of the planet. An accurate value of ν_0 would give us a measure of the radius of the core, and improve all known models of Jupiter.

Finally, it would be useful, if the previous two paths were taken, to repeat the entire analysis for the **entire** list of known or suspected Jovian p- and g-modes, based on the most current models. Direct communication with Mosser and Gudkova may be necessary to get these values, as they have not been published in the literature. Direct examination of each suspected mode, with a band-pass filter evaluation of the spectrum around it, may yield surprising results.

6.3 Conclusion

We have taken data recorded 30 years ago over 5 AU away. We cleaned, gap-filled, and filtered this data, and then analyzed it for evidence of Jovian modes. We found significant statistical evidence of free oscillations in the magnetic field around Jupiter, as can be seen in Table 5.10. We found evidence of p-modes propagating from Jupiter out toward the bow shock, and recorded significant values in Tables 5.8 and 5.9.

We evaluated independently the data before and after the bow shock, and concluded that the bow shock does act as a damper, effectively isolating the environment inside it as a model for Jovian modal structures.

We confirmed, in the same vein as Mosser *et al.* that the splitting between low-order modes is on the order of $\pm 110 - 130 \mu\text{Hz}$, which leads to an oscillation characteristic frequency (see [6]) of approximately $142 \pm 3 \mu\text{Hz}$.

We finally conclude that the magnetic field around Jupiter is **not** chaotic, and does represent a forced system in which there are readily identifiable modal structures, due in large part to the planet itself.

Chapter 7

Appendix

7.1 Table in Full

Table 7.1: F-test Results on the Closest Approach Data: 90% significance test on 6 sets. Analysis performed on zero-padded 8192-sample set. See Section 5.4 for truncated version of this table, with discussion.

Bin(s)	Frequency	B_x	B_y	B_z	$ B $
12	25.431 μHz	3	2	0	1
13	27.551 μHz	3	3	0	2
14	29.670 μHz	3	2	0	2
22	46.624 μHz	0	0	3	0
23	48.743 μHz	0	0	3	1
39	82.652 μHz	2	1	1	4
40	84.771 μHz	3	1	1	3
41	86.890 μHz	3	1	1	0
65	137.753 μHz	3	2	0	2
66	139.872 μHz	4	3	1	1
67	141.991 μHz	4	1	1	1
68	144.111 μHz	4	1	1	0

continued on next page

<i>Continued from previous page</i>						
Bin(s)	Frequency	B_x	B_y	B_z	$ B $	
119	252.194	μHz	0	0	0	3
121	256.432	μHz	0	1	0	3
123	260.671	μHz	0	2	0	3
124	262.790	μHz	0	2	1	3
182	385.708	μHz	0	0	2	3
183	387.828	μHz	0	0	4	3
184	389.947	μHz	0	0	2	3
228	483.195	μHz	0	0	0	3
231	489.553	μHz	0	0	3	0
266	563.727	μHz	0	4	1	1
267	565.847	μHz	0	2	1	3
268	567.966	μHz	1	2	1	3
314	665.453	μHz	1	3	0	2
336	712.077	μHz	0	1	0	3
337	714.196	μHz	0	1	1	3
360	762.939	μHz	0	0	3	0
367	777.774	μHz	3	0	0	0
385	815.921	μHz	0	3	1	1
456	966.390	μHz	1	2	3	0
457	968.509	μHz	1	0	3	0
469	993.940	μHz	1	1	0	3
470	996.060	μHz	0	0	1	3
504	1.068	mHz	0	0	3	1
505	1.070	mHz	0	0	3	0
522	1.106	mHz	3	0	1	1
547	1.159	mHz	2	2	3	1
567	1.202	mHz	3	0	0	1
568	1.204	mHz	3	1	0	0
625	1.325	mHz	0	0	3	2
645	1.367	mHz	2	1	0	3
661	1.401	mHz	1	1	1	3
662	1.403	mHz	0	1	1	3
663	1.405	mHz	0	0	2	3
688	1.458	mHz	1	0	2	3
689	1.460	mHz	0	0	3	2

continued on next page

<i>Continued from previous page</i>						
Bin(s)	Frequency		B_x	B_y	B_z	$ B $
694	1.471	mHz	3	0	0	1
763	1.617	mHz	0	2	3	0
829	1.757	mHz	1	0	3	0
848	1.797	mHz	0	1	3	1
869	1.842	mHz	2	0	1	3
871	1.846	mHz	3	0	1	1
881	1.867	mHz	0	3	1	0
882	1.869	mHz	0	3	1	0
927	1.965	mHz	1	1	3	1
928	1.967	mHz	0	1	3	2
938	1.988	mHz	0	3	0	1
939	1.990	mHz	1	3	1	1
970	2.056	mHz	1	3	0	0
972	2.060	mHz	0	1	0	3
973	2.062	mHz	0	0	0	3
985	2.087	mHz	0	0	3	1
998	2.115	mHz	0	3	0	0
1002	2.124	mHz	3	0	0	1
1025	2.172	mHz	1	0	3	2
1031	2.185	mHz	0	3	0	0
1032	2.187	mHz	1	3	0	0
1055	2.236	mHz	3	0	2	1
1056	2.238	mHz	2	1	3	0
1077	2.282	mHz	0	1	1	3
1088	2.306	mHz	3	2	0	0
1100	2.331	mHz	1	1	0	3
1101	2.333	mHz	1	1	3	3
1102	2.335	mHz	1	0	3	1
1103	2.338	mHz	0	0	3	1
1109	2.350	mHz	3	0	1	1
1110	2.352	mHz	3	1	0	1
1111	2.355	mHz	3	0	0	0
1119	2.371	mHz	0	1	1	3
1130	2.395	mHz	1	1	3	1
1149	2.435	mHz	3	1	1	0

continued on next page

<i>Continued from previous page</i>						
Bin(s)	Frequency		B_x	B_y	B_z	$ B $
1170	2.480	mHz	0	2	3	2
1171	2.482	mHz	1	1	3	2
1199	2.541	mHz	0	2	3	2
1261	2.672	mHz	0	0	3	2
1262	2.675	mHz	0	3	3	2
1263	2.677	mHz	0	2	3	3
1270	2.691	mHz	3	1	0	1
1284	2.721	mHz	1	0	3	1
1285	2.723	mHz	1	0	3	1
1286	2.725	mHz	1	0	3	2
1287	2.728	mHz	0	0	1	4
1288	2.730	mHz	0	1	1	3
1302	2.759	mHz	0	0	2	4
1303	2.761	mHz	0	0	1	4
1333	2.825	mHz	0	3	0	0
1334	2.827	mHz	0	3	0	0
1340	2.840	mHz	3	0	2	0
1341	2.842	mHz	2	0	4	1
1342	2.844	mHz	1	0	3	2
1343	2.846	mHz	0	0	3	2
1344	2.848	mHz	1	0	3	2
1369	2.901	mHz	3	0	0	1
1432	3.035	mHz	3	0	2	0
1433	3.037	mHz	3	0	3	0
1440	3.052	mHz	0	3	1	2
1441	3.054	mHz	0	3	1	1
1442	3.056	mHz	0	3	1	0
1530	3.242	mHz	3	0	1	0
1550	3.285	mHz	3	0	1	0
1564	3.315	mHz	1	0	1	3
1565	3.317	mHz	1	1	1	3
1571	3.329	mHz	3	1	0	0
1615	3.423	mHz	0	1	1	3
1616	3.425	mHz	0	1	1	3
1655	3.507	mHz	3	1	1	2

continued on next page

<i>Continued from previous page</i>						
Bin(s)	Frequency		B_x	B_y	B_z	$ B $
1656	3.510	mHz	1	1	0	3
1706	3.615	mHz	1	1	0	3
1707	3.618	mHz	1	0	0	3
1726	3.658	mHz	0	1	1	3
1727	3.660	mHz	0	2	0	3
1754	3.717	mHz	1	3	0	0
1835	3.889	mHz	3	2	0	1
1837	3.893	mHz	0	3	0	0
1904	4.035	mHz	0	1	3	2
1905	4.037	mHz	0	1	3	2
1906	4.039	mHz	0	1	3	2
1910	4.048	mHz	0	1	0	3
1911	4.050	mHz	1	0	0	3
1937	4.105	mHz	0	3	0	1
1938	4.107	mHz	0	3	0	1
1939	4.109	mHz	1	3	0	0
1959	4.152	mHz	1	3	0	0
1982	4.200	mHz	3	0	0	0
2001	4.241	mHz	3	2	2	1
2015	4.270	mHz	0	3	0	0
2024	4.289	mHz	1	0	3	0
2038	4.319	mHz	0	1	3	1

Bibliography

- [1] A.Cacciani, M.Dolci, P.F.Moretti, F.D'Alessio, C.Giuliani, E.Micolucci, and A.Di Cianno. Search for global oscillations on Jupiter with a double-cell sodium magneto-optical filter. *Astronomy and Astrophysics*, 372:317–325, 2001.
- [2] George Backus and Freeman Gilbert. The rotational splitting of the free oscillations of the Earth. *Proceedings of the National Academy of Science*, pages 362–371, 1961.
- [3] D. Bercovici and G. Schubert. Jovian Seismology. *Icarus*, 69:557–565, 1987.
- [4] B.Mosser, D.Gautier, and Ph.Delache. Oscillations of Jupiter as a Tool for Probing Its Internal Structure. *Proc. Symp. Seismology of the Sun and Sun-like Stars*, pages 593–594, 1988.
- [5] B.Mosser, D.Mekarnia, J.P.Maillard, J.Gay, D.Gautier, and P.Delache. Seismological observations with a Fourier transform spectrometer: detection of Jovian oscillations. *Astronomy and Astrophysics*, 267:604–622, 1993.
- [6] B.Mosser, J.P.Maillard, and D.Mekarnia. New attempt at detecting the Jovian oscillations. *Icarus*, 144:104–113, 2000.
- [7] D. R. Brillinger. *Time Series: Data Analysis and Theory*. SIAM, 2001.

- [8] Jorgen Christensen-Dalsgaard, Douglas Gough, , and Juri Toomre. Seismology of the Sun. *Science*, 229:923–931, 1985.
- [9] J.E.P. Connerney. Magnetic fields of the outer planets. *Journal of Geophysical Research*, 98:18659–18679, 1993.
- [10] Harold Cramér. *Mathematical Methods of Statistics*. Princeton University Press, 1961.
- [11] R.A. Davis and P.J. Brockwell. *Time Series: Theory and Methods*. Springer-Verlag, 1991.
- [12] R. Deutsch. *Estimation Theory*. Prentice-Hall, 1965.
- [13] B. Dintrans and R.Ouyed. On Jupiter’s inertial mode oscillations. *Astronomy and Astrophysics*, 375:L47–L50, 2001.
- [14] D. Deming et al. A search for P-mode Oscillations of Jupiter - Serendipitous observations of nonacoustic thermal wave structure. *Astrophysical Journal*, 343:456, 1989.
- [15] N. Ness et al. Magnetic Field Studies at Jupiter by Voyager 2: Preliminary Results. *Science*, 206:966–972, 1979.
- [16] William H. Press et al. *Numerical Recipes in FORTRAN 77 - The Art of Scientific Computing*. Cambridge University Press, 1986.
- [17] John E. Freund. *Mathematical Statistics*. Prentice-Hall, 1962.
- [18] M. Goossens and P. Smeyers. Gravity modes in composite polytropic stars. *Astrophysics and Space Science*, 26:137–151, 1973.

- [19] T.V. Gudkova and V.N.Zharkov. The free oscillations of Jupiter. *Planetary and Space Science*, 47:1211–1224, 1999.
- [20] William C. Guenther. *Analysis of Variance*. Prentice-Hall Inc., 1964.
- [21] Charles A. Higgins, Thomas D. Carr, and Francisco Reyes. A new determination of Jupiter’s radio rotation period. *Geophysical Research Letters*, 23:104–113, 2000.
- [22] D.E. Huddleston, C.T. Russell, M.G. Kivelson, K.K. Khurana, and L. Bennett. Location and shape of the Jovian magnetopause and bow shock. *JGR-Planets*, 103:20075, 1998.
- [23] Donald M. Hunten, William F. Hoffmann, and Ann L. Sprague. Jovian seismic waves and their detection. *Geophysical Research Letters*, 21:1091–1094, 1994.
- [24] Umin Lee. Acoustic Oscillations of Jupiter. *The Astrophysical Journal*, 405:359–374, 1993.
- [25] K.S. Miller. Complex Linear Least Squares. *SIAM Review*, 15:706–726, 1973.
- [26] B. Mosser, P. Gaulme, and The Jovis Team. Jovis: Jupiter, Oscillation, Variability, Interior Structure. Semaine de l’Astrophysique Francaise, EdP-Sciences, Jun 2004.
- [27] B. Mosser, F.X. schmider, Ph. Delache, and D. Gautier. A possible detection of Jovian global oscillations. *Astronomy and Astrophysics*, 251:356–364, 1991.
- [28] Benoit Mosser. The pressure mode oscillation spectrum of a rotating gaseous sphere: Application to Jupiter. *Icarus*, 87:198–209, 1990.

- [29] Benoit Mosser, Daniel Gautier, and Theodor Kostiuk. On the detectability of Jovian Oscillations with infrared heterodyne measurements. *Icarus*, 96:51–26, 1992.
- [30] Donald B Percival and Andrew T. Walden. *Spectral Analysis for Physical Applications*. Cambridge University Press, 1993.
- [31] German Pietro. *Improving Earthquake Source Spectrum Estimation using Multitaper Techniques*. PhD thesis, University of California, San Diego, April 2007.
- [32] H. Press and J.W. Tukey. Power Spectral Methods of Analysis and Application in Airplane Dynamics. In E.J Durbin, editor, *AGARD Flight Test Manual, Vol. IV, Instrumentation*, page C1:C41. Paris: NATO, Advisory Group for Aeronautical Research and Development, 1956.
- [33] M.B. Priestley. *Spectral Analysis and Time Series*. Elsevier Academic Press, 1981.
- [34] J. Provost, B. Mosser, and G. Berthomieu. A new asymptotic formalism for Jovian seismology. *Astronomy and Astrophysics*, 274:595–611, 1993.
- [35] J.A. Rice. *Mathematical Statistics and Data Analysis*. Duxbury Bress, second edition, 1995.
- [36] FX Schmider, B.Mosser, and E.Fossat. Possible Detection of Jovial global oscillations. *Astronomy and Astrophysics*, 248:281–291, 1991.
- [37] D. Slepian. Prolate spheroidal wave functions, Fourier analysis, and uncertainty-v: The discrete case. *Bell Systems Technical Journal*, 57:1371–1429, 1978.

- [38] Monique Tassoul. Asymptotic Approximations for Stellar Nonradial Pulsations. *The Astrophysical Journal Supplement Series*, 43:469–490, 1980.
- [39] D. J. Thomson. Multitaper analysis of nonstationary and nonlinear time series data. In A.W.W.J. Fitzgerald, R.L. Smith, and P. Young, editors, *Nonlinear and Nonstationary Signal Processing*, pages 317–394. Cambridge University Press, 2000.
- [40] David J. Thomson. Spectrum Estimation and Harmonic Analysis. *Proceedings of the IEEE*, 79:1055–1095, 1982.
- [41] D.J. Thomson. Scientific spectrum estimation: Advanced multitaper methods of time-series analysis. 2006.
- [42] D.J. Thomson, L.J.Lanzerotti, and C.G. Maclellan. Interplanetary magnetic field: Statistical properties and discrete modes. *Journal of Geophysical Research*, 106:15941–15962, 2001.
- [43] D.J. Thomson, C.G. Maclellan, and L.J.Lanzerotti. Propagation of solar oscillations through the interplanetary medium. *Nature*, 376:139–144, 1995.
- [44] W.B.Hubbard V.P. Trubitsyn and V.N.Zharkov. Significance of Gravitational Moments for Interior Structure of Jupiter and Saturn. *Icarus*, 21:147–151, 1974.
- [45] S.V. Vorontsov, V.N. Zharkov, and V.M.Lubimov. The Free Oscillations of Jupiter and Saturn. *Icarus*, 27:109–118, 1976.
- [46] A. Yaglob. *An Introduction to the Theory of Stationary Random Functions*. Dover, 1973.